

Final Report for AOARD Grant FA23861014049
“Metal Nanostructures for Detection and Imaging Enhancements”

January 3, 2011

Name of Principal Investigators: Chih-Chung (C. C.) Yang

- e-mail address : ccy@cc.ee.ntu.edu.tw
- Institution : Graduate Institute of Photonics and Optoelectronics, National Taiwan University
- Mailing Address : No. 1, Roosevelt Road, Section 4, Taipei, 10617 Taiwan
- Phone : 886-2-23657624
- Fax : 886-2-23652637

Period of Performance: 01/01/2010– 12/31/2010

Table of Contents:

Abstract	p. 2
Part I: Au Nanorings for Enhancing Absorption and Backscattering at Localized Surface Plasmon Resonance	p. 3
Part II: Absorption enhancement of an amorphous Si solar cell through surface plasmon-induced scattering with metal nanoparticles	p. 15
Part III: Surface Plasmon Coupling with a Radiating Dipole	p. 29
List of Related Journal Publications:	p. 35
Future Work	p. 36

Report Documentation Page				Form Approved OMB No. 0704-0188	
Public reporting burden for the collection of information is estimated to average 1 hour per response, including the time for reviewing instructions, searching existing data sources, gathering and maintaining the data needed, and completing and reviewing the collection of information. Send comments regarding this burden estimate or any other aspect of this collection of information, including suggestions for reducing this burden, to Washington Headquarters Services, Directorate for Information Operations and Reports, 1215 Jefferson Davis Highway, Suite 1204, Arlington VA 22202-4302. Respondents should be aware that notwithstanding any other provision of law, no person shall be subject to a penalty for failing to comply with a collection of information if it does not display a currently valid OMB control number.					
1. REPORT DATE 21 JAN 2011		2. REPORT TYPE Final		3. DATES COVERED 11-02-2011 to 10-02-2011	
4. TITLE AND SUBTITLE Metal Nanostructures for Detection and Imaging Enhancements				5a. CONTRACT NUMBER FA23861014049	
				5b. GRANT NUMBER	
				5c. PROGRAM ELEMENT NUMBER	
6. AUTHOR(S) Chih-Chung Yang				5d. PROJECT NUMBER	
				5e. TASK NUMBER	
				5f. WORK UNIT NUMBER	
7. PERFORMING ORGANIZATION NAME(S) AND ADDRESS(ES) National Taiwan University, Institute of Electro-Optical Engineering, Room 445, Taipei 10617, Taiwan, NA, NA				8. PERFORMING ORGANIZATION REPORT NUMBER N/A	
9. SPONSORING/MONITORING AGENCY NAME(S) AND ADDRESS(ES) AOARD, UNIT 45002, APO, AP, 96338-5002				10. SPONSOR/MONITOR'S ACRONYM(S) AOARD	
				11. SPONSOR/MONITOR'S REPORT NUMBER(S) AOARD-104049	
12. DISTRIBUTION/AVAILABILITY STATEMENT Approved for public release; distribution unlimited					
13. SUPPLEMENTARY NOTES					
14. ABSTRACT This is the report of a project to 1) create a high concentration of Au nanorings as image contrasting agents, 2) deposit metal nanoparticles in amorphous Si solar cells for absorption enhancement, and 3) simulate enhanced radiated power of a dipole when it is coupled with the localized surface plasmon resonance of a nearby metal nanosphere.					
15. SUBJECT TERMS Metal Nanoparticles, Surface Plasmon Resonance, Detector Technology, Imaging					
16. SECURITY CLASSIFICATION OF:			17. LIMITATION OF ABSTRACT Same as Report (SAR)	18. NUMBER OF PAGES 35	19a. NAME OF RESPONSIBLE PERSON
a. REPORT unclassified	b. ABSTRACT unclassified	c. THIS PAGE unclassified			

Abstract:

This research report includes three parts. First, preparation of a high-concentration Au nanoring (NR) water solution and its applications to the enhancement of image contrast in optical coherence tomography (OCT) and the generation of photothermal effect in a sample through localized surface plasmon (LSP) resonance are demonstrated. Au NRs are first fabricated on a sapphire substrate with colloidal lithography and secondary sputtering of Au, and then transferred into water solution through a liftoff process. By controlling the NR geometry, the LSP dipole resonance wavelength in tissue can cover the spectral range of 1300 nm for OCT scanning of deep tissue penetration. The extinction cross sections of the fabricated Au NRs in water are estimated to give the levels of 10^{-10} - 10^{-9} cm² near their LSP resonance wavelengths. The fabricated Au NRs are then delivered into pig adipose samples for OCT scanning. It is observed that when resonant Au NRs are delivered into such a sample, LSP resonance-induced Au NR absorption results in a photothermal effect, making the opaque pig adipose cells transparent. Also, the delivered Au NRs in the intercellular substance enhance the image contrast of OCT scanning through LSP resonance-enhanced scattering. By continuously OCT scanning a sample, both photothermal and image contrast enhancement effects are observed. However, by continually scanning a sample with a low scan frequency, only the image contrast enhancement effect is observed.

Second, the simulation results of absorption enhancement in an amorphous-Si (a-Si) solar cell by depositing metal nanoparticles (NPs) on the device top and embedding metal NPs in a layer above the Al back-reflector are demonstrated. The absorption increase results from the near-field constructive interference of electromagnetic waves in the forward direction such that an increased amount of sunlight energy is distributed in the a-Si absorption layer. Among the three used metals of Al, Ag, and Au, Al NPs show the most efficient absorption enhancement. Between the two used NP geometries, Al nanocylinder (NC) are more effective in absorption enhancement than Al nanosphere (NS). Also, a random distribution of isolated metal NCs can lead to higher absorption enhancement, when compared with the cases of periodical metal NC distributions. Meanwhile, the fabrication of both top and bottom Al NCs in a solar cell results in further absorption enhancement. Misalignments between the top and bottom Al NCs do not significantly reduce the enhancement percentage. With a structure of vertically aligned top and bottom Al NCs, solar cell absorption can be increased by 52 %.

Third, the simulation results of the enhanced radiated power of a radiating dipole when it is coupled with the localized surface plasmon resonance (LSPR) of a nearby metal nanosphere (NS) by including the influence of the LSPR on the strength of the dipole, which is represented by a two-level system in our semi-classical model, are demonstrated. It is shown that with this feedback influence, the total radiated power can be further enhanced by more than several tens percents, when compared with the condition of ignoring the feedback effect. In comparing the results of two different dipole orientations, it is discovered that at a fixed distance from the metal NS, the radial dipole orientation leads to more significant enhancement of total radiated power, when compared to the orbital dipole orientation.

Part I: Au Nanorings for Enhancing Absorption and Backscattering at Localized Surface Plasmon Resonance

1. Introduction

With its unique scattering and absorption features near resonance, localized surface plasmon (LSP) induced on a metal nanoparticle (NP) has found broad applications in emission and absorption enhancements [1-5], biomedical imaging contrast improvement [6-10], and photothermal therapy [11-14]. Among various metals for fabricating NPs for biomedical applications, Au is preferred due to its biocompatibility. By connecting the anti-body of targeted cells to Au NPs through a bio-conjugation process, the NPs can attach the targeted cells and possibly be internalized into cells when they are delivered into bio-tissue. In optical imaging of bio-tissue, the strong scattering of the Au NPs around the LSP resonance wavelength can lead to a higher image contrast of the targeted cells. Also, the strong LSP absorption results in local heating in the tissue and can cause the death of targeted cells, leading to the effect of photothermal therapy. For such biomedical applications, the widely used Au NPs include nanorods [15-17], nanoshells [18-20], and nanocages [21-23]. However, most of the LSP resonance wavelengths of those reported Au NPs are shorter than 1000 nm. From the viewpoint of optical imaging application, particularly of optical coherence tomography (OCT), although a shorter wavelength around 800 nm can lead to higher imaging resolution, the use of a light source of a longer wavelength around 1300 nm can result in deeper tissue penetration due to weaker tissue scattering. The issue of deeper tissue penetration of light is important not only for imaging but also for photothermal therapy. Although an Au nanorod of a larger aspect ratio can push the LSP resonance wavelength into the spectral range around 1300 nm, it is usually difficult to control the uniformity of nanorods and hence the application becomes unreliable. Also, although theoretically nanoshells and nanocages of thin Au layers can lead to LSP resonances at longer wavelengths, the non-uniform shell/wall thickness results in significantly broadened and hence weaker resonance peaks. Reliable Au NPs of other geometries for longer-wavelength and stronger LSP resonance are needed for further developments of targeted optical imaging and photothermal therapy. For this purpose, Au nanoring (NR) shows the advantage of long-wavelength LSP resonance. The fabrication of Au NRs on a substrate has been reported based on the methods of colloidal lithography and secondary sputtering of metal [24-26]. However, the delivery of such Au NRs into tissues or cells for optical imaging, therapy, and other biomedical applications has not yet been reported.

In this part of report, we report the fabrication of Au NRs on sapphire substrate using the methods of colloidal lithography and secondary sputtering of Au and the development of a process for NR liftoff from the substrate. The aqueous solution of Au NRs is prepared for measuring the LSP resonance properties. The results agree reasonably well with those of numerical simulations. The Au NRs are then delivered into pig adipose samples for OCT scanning to demonstrate the enhanced absorption and scattering behaviors of LSP resonance. It is observed that when the LSP resonance wavelength coincides with the OCT light source spectrum, the resonant Au NRs lead to the heating of adipose cells and higher image contrast. Such features are not observed when another Au NR sample, in which the LSP resonance wavelength significantly deviates from the OCT light source spectrum, is delivered into a pig adipose sample. OCT is a widely used optical imaging technique for the diagnoses of many diseases [27-29], including early-diagnosis of oral cancer and precancer [30-32]. It is based on the principle of low-coherence interferometry. In most human tissue, OCT scanning can lead to high-resolution imaging with a depth of 2-3 mm, showing its most advantageous feature when compared with optical microscopy techniques. With a light source of >100 nm in spectral width within the spectral window of 700-1350 nm, the tissue resolution can be higher than 7 microns. With the interferometry nature of OCT and the coherent property of LSP-induced scattering of Au NPs, OCT represents an effective approach for monitoring the LSP-induced functions in bio-tissue.

This part of report is organized as follows: In Section 2, the procedures of fabricating Au NRs on sapphire substrate and then in aqueous solution are described. The measured and simulated LSP resonance properties of the fabricated Au NRs are demonstrated in Section 3. Next, OCT scanning images created by delivering Au NRs into pig adipose samples are shown and discussed in Section 4. Finally, conclusions are drawn in Section 5.

2. Fabrication of Au Nanorings

The fabrication of Au NRs starts with a colloidal lithography process through electrostatic adsorption of polystyrene colloidal particles (Duke Scientific Corporation) on a SiO₂ layer of 20 nm in thickness

[33], which is coated on a sapphire substrate with plasma-enhanced chemical vapor deposition. Two samples are prepared with colloidal particle diameters at 150 (sample A) and 100 (sample B) nm. Then, an Au film ~30 nm in thickness is deposited on top of the substrate to serve as the source of secondary sputtering. Next, reactive ion etching (RIE) is applied by using CHF_3 as etchant for forming Au ring structures around the colloidal particles through the processes of secondary sputtering and removing the rest Au atoms. During the RIE process, the colloidal particles are partially etched. An O_2 plasma etching procedure completely cleans the colloidal particle material, leaving Au NRs on SiO_2 -deposited sapphire substrate. A typical scanning electron microscopy (SEM) image of the Au NRs of sample A on the SiO_2 -deposited sapphire substrate is shown in Fig. 1. Here, the average outer diameter of those Au NRs is about 174 nm with the inner diameter at ~150 nm since Au atoms are sputtered onto the sidewall of a colloidal particle. Therefore, the average thickness of the NRs is about 12 nm. The average outer diameter of the Au NRs of sample B is about 118 nm with the average Au thickness at ~9 nm.

The Au NRs are then surface modified by APTS ((3-aminopropyl) trimethoxysilane, 97%, Alfa Aesar) to prevent them from aggregation in water. In this process, a 1:1 water-ethanol solution (100 mL) is combined with 50 μL of APTS, and is maintained at pH 10 by adding NH_3 solution. The substrate samples are immersed in this mixture for more than 24 hours and, subsequently, are rinsed with ethanol and dried with N_2 flow. To transfer the substrate-attached Au NRs into water solution, the substrate samples are immersed in a KOH solution (85%, 13.6% w.t. in water) for 15 min to etch the SiO_2 layer between Au NRs and sapphire substrate, followed by a step of gentle rinse with de-ionized water to remove residual KOH. Then, the substrate sample is placed in a glass bottle filled with the proper amount of de-ionized water. After sonication, the Au NRs are transferred into water solution. To increase the stability of NRs, PEG-Thiol (mPEG-Thiol-5000, Laysan Bio Inc., Arab, AL) is added to the NR solution to reach a concentration of 2.5×10^{-5} M. The mixture is then incubated at room temperature for 20 hours. To deliver the NRs into tissue for OCT scanning, the NR solution is centrifuged to give a higher particle concentration. Figure 2 shows a plan-view SEM image of Au NRs of sample A after liftoff. The SEM image was taken when the dried Au NRs are placed on a Si substrate. Here, one can see that the inner and outer diameters of the NRs change slightly along their ring axes.

3. Surface Plasmon Characteristics of Au Nanorings

Optical transmissions of the water solutions of Au NRs are measured with a UV-vis spectrophotometer (Jasco V-570) to show the normalized extinction spectra in Fig. 3 (the left ordinate). Here, one can see the major peaks of extinction, corresponding to the LSP dipole resonances in water, at 1240 and 1030 nm for samples A and B, respectively. In this figure, the spectrum of the sweeping-frequency laser source of the used OCT system is also shown for comparison (the right ordinate). The light source spectrum with its peak at 1310 nm and spectral full-width at half-maximum at ~100 nm is covered by the long-wavelength side of the LSP dipole resonance range of sample A. However, the LSP dipole resonance range of sample B is quite far away from the OCT light source spectrum. The secondary peaks of the extinction spectra in Fig. 3 correspond to the mixture of the higher-order resonance across the ring and the resonance along the ring axis (see the discussions for Figs. 4 and 5).

To further understand the resonance behaviors of the fabricated Au NRs, numerical simulations based on the finite-element method are performed by assuming an ideal ring shape shown in the insert of Fig. 4. In Fig. 4, the extinction spectra of the Au NRs are obtained with the excitation light incident along the z axis and incident linear polarization in the y direction. Here, the normalized extinction spectra of the two samples with ambient refractive indices at 1.33 (corresponding to NRs in water – curves A(1.33) and B(1.33)) and 1.4 (corresponding to NRs in tissue – curves A(1.4) and B(1.4)) are shown. The used NR parameters include the outer diameter at 179 (120) nm, inner diameter at 149 (97) nm, and height at 95 (60) nm for sample A (B). For simulations, the dispersive dielectric constant of Au follows the experiment data in ref. [34]. Although the SEM image in Fig. 2 shows that the diameter of an NR changes along its axis, the numerical results in Fig. 4 show the reasonable agreements of LSP resonance spectra with the measurements. In Fig. 4, one can also see that by increasing the ambient refractive index, the LSP resonance wavelengths are red shifted. In this situation, the spectral range of the LSP dipole resonance of sample A completely covers the OCT light source spectrum. Meanwhile, that of sample B only slightly overlaps with the OCT light source spectrum. Therefore, it is expected that only sample A can significantly induce LSP

resonance-enhanced backscattering and absorption in bio-tissue. It is noted that the extinction spectra obtained from water solution measurements shown in Fig. 3 are significantly broader than their counterparts obtained from single-NR simulations shown in Fig. 4. This difference can be attributed to (1) the non-uniform shape and size distributions among different NRs, (2) the random orientation distribution of Au NRs in water solution, and (3) the possible LSP coupling between neighboring NRs in water solution.

For further understanding the LSP resonance properties of the fabricated Au NRs in water solution, we also evaluate the extinction spectra of LSP resonances across the ring and along the ring axis by assuming that the excitation light is incident along the y-axis and the incident linear polarizations are in the x and z directions, respectively. Figure 5 shows the simulation results of the two samples, including the resonances across the ring (curves A/ring and B/ring) and those along the ring axis (curves A/axis and B/axis). In the curves for the resonances across the ring, one can see the major peaks of dipole resonance the same as those shown in Fig. 4. The minor peaks at shorter wavelengths correspond to higher-order resonance modes. The combination of the higher-order cross-ring resonance mode with LSP modes along the ring axis corresponds to the secondary peaks between 500 and 900 nm in Fig. 3. The data shown in Fig. 3 represent the total resonance effect of numerous Au NRs of random orientation distributions in water.

The accurate evaluation of NP concentration in solution still represents a major problem in the development of Au NP application. The NR concentration in water solution can be estimated by first counting the Au NR surface density on sapphire substrate based on the statistics of SEM observations to give $1.44 \times 10^9 \text{ cm}^{-2}$ for sample A and $2.64 \times 10^9 \text{ cm}^{-2}$ for sample B. This surface density is multiplied by the substrate area (a quarter of a 2-inch sapphire substrate) to give the total NR numbers on a substrate at 7.29×10^9 NRs for sample A and 1.34×10^{10} NRs for sample B. These Au NRs are transferred into a water solution of 4 mL in volume to give particle concentrations of 1.82×10^9 and $3.35 \times 10^9 \text{ cm}^{-3}$ for samples A and B, respectively. It is noted that in this concentration estimation procedure, errors can be made through inaccuracy in evaluating the NR surface density on substrate and NR loss in transferring NRs into water solution. Therefore, the NR concentrations of samples A and B are estimated to be $\sim 1.09 \times 10^9$ and $\sim 2.01 \times 10^9 \text{ cm}^{-3}$, respectively, by assuming that 40 % NRs are lost in the process of transferring NRs into water solution. The water solutions of the two samples are then condensed by a factor of about 12 to give the final concentrations of $\sim 1.31 \times 10^{10}$ and $\sim 2.41 \times 10^{10} \text{ cm}^{-3}$ in samples A and B, respectively, for OCT scanning application. We also use the method of inductively coupled plasma mass spectrometry for estimating the NR concentrations to give 1.07×10^{10} and $3.58 \times 10^{10} \text{ cm}^{-3}$ for samples A and B, respectively, after condensation. Considering all the inaccuracies in measurements and estimations, we suppose that these results agree reasonably well with the aforementioned values obtained from surface density estimation.

The extinction cross sections of the NRs can be evaluated based on transmission measurement. By using the NR solutions before condensation, we obtained the transmittances of 54.58 and 56.47 % through the solutions of 1 cm in length for samples A and B, respectively, at their individual resonance wavelengths, i.e., at 1240 and 1030 nm for samples A and B, respectively. From the measurement results, we can obtain the NR extinction cross sections of 5.56×10^{-10} and $2.84 \times 10^{-10} \text{ cm}^2$ for samples A and B, respectively, at their individual resonances. Figure 6 shows the extinction (Ext), scattering (Sca), and absorption (Abs) cross sections of single Au NRs in water as functions of wavelength for samples A and B obtained from numerical simulations. Here, one can read the extinction cross sections of 3.13×10^{-9} and $1.70 \times 10^{-9} \text{ cm}^2$ at individual resonance wavelengths for samples A and B, respectively. The simulation results of single NRs are about 5.8 times those from transmission measurement. Several reasons can be used for explaining this difference, including (1) the non-uniform size and geometry distributions of NRs (leading to the reduction of overall resonance strength and broadening of resonance spectrum), (2) the random orientation distribution of NRs (resulting in weaker overall resonance strength), (3) the difficulty of accurately evaluating NR concentration (underestimating the extinction cross section based on transmission measurement), and (4) the possibility of LSP coupling between neighboring NRs (also leading to the reduction of overall resonance strength and broadening of resonance spectrum). In Fig. 6, it is noted that the spectral peaks of scattering and absorption cross sections are slightly different in both samples. Also, scattering is significantly stronger than absorption in sample A. However, scattering and absorption strengths become comparable in sample B.

4. Optical Coherence Tomography Images

In the used OCT system, a sweeping-frequency laser source with the output spectrum shown in Fig. 3 is used as the light source. The light source is connected to a Mech-Zehnder interferometer, which consists of two optical couplers and two circulators. The interference fringe signal is detected by a balanced photo-detector and sampled by a high-speed digitizer. The achieved system sensitivity and axial resolution in tissue are 103 dB and 6 μm at the depth of 1 mm, respectively. The detailed descriptions about the OCT system and its operation condition can be found in ref. [32].

Although the photothermal effect generated by LSP resonance of Au NP has been widely observed, the measurement of local temperature variation in a bio-sample is still difficult. To demonstrate the effects of LSP resonance-enhanced scattering and absorption in bio-tissue, we chose pig adipose as our sample for OCT scanning. Pig adipose cells of 100-200 μm in size are opaque in the visible-near-infrared range at a temperature lower than 25 $^{\circ}\text{C}$. When such a cell is heated to reach a higher temperature, it becomes transparent [35]. Therefore, pig adipose can be used for demonstrating the local heating effect through LSP resonance. In our experiment, fresh pig adipose samples are refrigerated before OCT scanning. After removing a sample from the refrigerator, it takes about four hours to observe transparent cells at the ambient temperature of 25 $^{\circ}\text{C}$. Figures 7(a)-7(d) show the OCT scanning images at the same location of a pig adipose sample before, 0 min, 30 min, and 60 min after the application of a water solution droplet of non-resonant Au NRs (sample B) onto the sample surface, respectively. The OCT scanning experiment was started right after the sample was moved out from the refrigerator. The sample was continuously scanned with the OCT system (about 15 scans per sec). In Fig. 7(b), one can clearly see the backscattering of Au NRs in the water solution droplet. The broad resonance spectrum of sample B shown in Fig. 3 partially overlaps with the OCT light source spectrum, leading to observable LSP resonance-induced backscattering in OCT scanning. After the non-resonant Au NRs are delivered into the adipose sample, as shown in Figs. 7(c) and 7(d), one can hardly observe any change in the OCT image from that before the application of non-resonant Au NRs.

The OCT scanning results with resonant Au NRs are quite different. Figures 8(a)-8(d) show the OCT scanning images at the same location of a pig adipose sample before, 0 min, 30 min, and 60 min after the application of a water solution droplet of resonant Au NRs (sample A) onto the sample surface, respectively. The sample was continuously scanned with the OCT system. In Fig. 8(b), one can see the significantly stronger backscattering signal from the water solution droplet, when compared with that in Fig. 7(b). By observing Figs. 8(c) and 8(d) closely, dark-hole structures of 100-200 μm in size (transparent adipose cells) can be seen. The adipose images in Figs. 8(c) and 8(d) are unclear because the Au NRs accumulated on the sample surface block the incident light in OCT scanning, as demonstrated by the thick bright surface boundaries in the figures. Figure 8(e) shows the OCT image around 60 min after the application of Au NR solution when a pure water droplet is used to wash out the accumulated Au NRs on the surface. Here, clear hole structures showing transparent adipose cells can be seen, indicating the local heating effect due to LSP resonance-induced absorption of Au NRs. Since the cells look so transparent, it is believed that most of the Au NRs are delivered into the intercellular substance for enhancing the cell imaging contrast in OCT scanning. The image contrast enhancement with resonant Au NRs can be observed by comparing Figs. 9(a) with 9(b). Figure 9(a) is a duplicate of Fig. 7(e) except that a horizontal dashed line is drawn for OCT signal intensity demonstration (see Fig. 10). The OCT scanning image in Fig. 9(b) is obtained by scanning a fresh pig adipose sample (without being refrigerated or using any Au NR). Here, although the hole structures can be clearly seen in Fig. 9(b), its image contrast is lower. The OCT lateral line-scan signal intensity distributions along the horizontal dashed lines in Figs. 9(a) and 9(b) are plotted in Fig. 10. Here, one can clearly see the enhanced image contrast after Au NRs are delivered into the adipose sample. Therefore, one can realize the effect of enhanced scattering due to LSP resonance besides the photothermal effect for making the adipose cell transparent.

The results shown in Figs. 7-10 are obtained from the experiments of continuously scanning the samples with the OCT system. In each OCT scan, the incident light can produce heating due to LSP-resonance-induced absorption enhancement. Therefore, we have observed a combined effect of enhanced absorption and scattering. To independently observe the LSP-resonance-induced scattering enhancement, we can minimize the photothermal effect by continually scanning the sample with a low scan frequency. Figures 11(a)-11(d) show the OCT images of a pig adipose sample taken before, 0 min, 30 min, and 60 min after the application of a droplet of Au NR water solution of sample A, respectively, when the sample is scanned once every 30 min such that the photothermal effect is minimized. Figure 11(e) shows the image similar to that in Fig. 11(d) after the Au NRs accumulated

on the surface are washed out. The pig adipose sample was refrigerated before the OCT scanning experiment. Here, one can see that adipose cells remain opaque through the 60-min period of experiment, implying that the photothermal effect is essentially deleted. Although the adipose cells are opaque, their boundaries can still be seen with OCT scanning. Such boundaries correspond to the sharp peaks in Fig. 12, in which two OCT line-scan intensity distribution curves along the vertical lines in Figs. 11(a) (Before) and 11(b) (Wash Out) are shown. Here, one can clearly see that after the delivery of resonant Au NRs into the intercellular substance of the adipose sample, the image contrast is enhanced under the condition of weak photothermal effect. The results shown in Figs. 11 and 12 clearly demonstrate the effect of enhanced image contrast. It is noted that the intensity levels in Figs. 10 and 12 are obtained from different image process procedures and their comparison does not make any sense.

5. Conclusions

In summary, the preparation of Au NR water solution of high concentration and their applications to the enhancement of image contrast in OCT and the generation of photothermal effect in bio-tissue have been demonstrated. Au NRs were first fabricated on sapphire substrate with colloidal lithography and secondary sputtering of Au, and then transferred into the water solution through a liftoff process. By controlling the NR geometry, the LSP dipole resonance wavelength in tissue could cover the spectral range around 1300 nm for OCT scanning of deep tissue penetration. The extinction cross sections of the fabricated Au NRs in water at their LSP resonance wavelengths were calibrated to give an order of magnitude of 10^{-10} - 10^{-9} cm². The fabricated Au NRs were delivered into pig adipose samples for OCT scanning. It was observed that when resonant Au NRs were delivered into such a sample, LSP resonance-induced Au NR absorption led to the photothermal effect of making the opaque pig adipose cells transparent. Also, the delivered Au NRs in the intercellular substance could enhance the image contrast of OCT scanning through LSP resonance-enhanced scattering. By continuously OCT scanning an adipose sample, both photothermal and image contrast enhancement effects could be observed. However, by continually OCT scanning a sample with a low scan frequency, only the image contrast enhancement effect could be seen.

References:

1. A. Neogi, C. W. Lee, H. O. Everitt, T. Kuroda, A. Tackeuchi, and E. Yablonvitch, *Phys. Rev. B* **66**, 153305 (2002).
2. G. Sun, J. B. Khurgin, and R. A. Soref, *Appl. Phys. Lett.* **90**, 111107 (2007).
3. D. M. Yeh, C. F. Huang, C. Y. Chen, Y. C. Lu, and C. C. Yang, *Nanotechnology* **19**, 345201 (2008).
4. V. E. Ferry, L. A. Sweatlock, D. Pacifici, and H. A. Atwater, *Nano Lett.* **8**, 4391-4397 (2008).
5. C. Rockstuhl and F. Lederer, *Appl. Phys. Lett.* **94**, 213102 (2009).
6. I. H. El-Sayed, X. Huang, and M. A. El-Sayed, *Nano Lett.* **5**, 829-834 (2005).
7. H. Ding, K. T. Yong, I. Roy, H. E. Pudavar, W. C. Law, E. J. Bergey, and P. N. Prasad, *J. Phys. Chem. C* **111**, 12552-12557 (2007).
8. E. V. Zagaynova, M. V. Shirmanova, M. Y. Kirillin, B. N. Khlebtsov, A. G. Orlova, I. V. Balalaeva, M. A. Sirotkina, M. L. Bugrova, P. D. Agrba, and V. A. Kamensky, *Phys. Med. Biol.* **53**, 4995-5009 (2008).
9. P. K. Jain, X. Huang, I. H. El-Sayed, and M. A. El-Sayed, *Accounts of Chemical Research* **41**, 1578-1586 (2008).
10. A. L. Oldenburg, M. N. Hansen, T. S. Ralston, A. Wei, and S. A. Boppart, *J. Mater. Chem.* **19**, 6407-6411 (2009).
11. X. Huang, P. K. Jain, I. H. El-Sayed, M. A. El-Sayed, *Lasers Med Sci* **23**, 217-228 (2008).
12. J. L. Li, D. Day, and M. Gu, *Adv. Mater.* **20**, 3866-3871 (2008).
13. X. Huang, I. H. El-Sayed, W. Qian, and M. A. El-Sayed, *J. Am. Chem. Soc.* **128**, 2115-2120 (2006).
14. S. Lal, S. E. Clare, and N. J. Halas, *Accounts Chem. Res.* **41**, 1842-1851 (2008).
15. M. Eghtedari, A. V. Liopo, J. A. Copland, A. A. Oraevsky, and M. Motamedi, *Nano Lett.* **9**, 287-291 (2009).
16. T. S. Troutman, J. K. Barton, and M. Romanowski, *Optics Lett.* **32**, 1438-1440 (2007).
17. G. von Maltzahn, J. H. Park, A. Agrawal, N. K. Bandaru, S. K. Das, M. J. Sailor, and S. N. Bhatia, *Cancer Res.* **69**, 3892-3900 (2009).
18. A. M Gobin, J. J Moon, J. L West, *International J. Nanomedicine* **3**, 351-358 (2008).

19. A. M. Gobin, M. H. Lee, N. J. Halas, W. D. James, R. A. Drezek, and J. L. West, *Nano Lett.* **7**, 1929-1934 (2007).
20. H. Liu, D. Chen, F. Tang, G. Du, L. Li, X. Meng, W. Liang, Y. Zhang, X. Teng, and Y. Li, *Nanotechnology* **19**, 455101 (2008).
21. J. Chen, D. Wang, J. Xi, L. Au, A. Siekkinen, A. Warsen, Z. Y. Li, H. Zhang, Y. Xia, and X. Li, *Nano Lett.* **7**, 1318-1322 (2007).
22. J. Chen, F. Saeki, B. J. Wiley, H. Cang, M. J. Cobb, Z. Y. Li, L. Au, H. Zhang, M. B. Kimmey, X. Li, and Y. Xia, *Nano Lett.* **5**, 473-477 (2005).
23. L. Au, D. Zheng, F. Zhou, Z. Y. Li, X. Li, and Y. Xia, *ACS Nano* **2**, 1645-1652 (2008).
24. E. M. Larsson, J. Alegret, M. Kall, and D. S. Sutherland, *Nano Lett.* **7**, 1256-1263 (2007).
25. F. Hao, E. M. Larsson, T. A. Ali, D. S. Sutherland, and P. Nordlander, *Chem. Phys. Lett.* **458**, 262-266 (2008).
26. J. Aizpurua, P. Hanarp, D. S. Sutherland, M. Kall, G. W. Bryant, and F. J. Garc a de Abajo, *Phys. Rev. Lett.* **90**, 057401 (2003).
27. D. Huang, E. A. Swanson, C. P. Lin, J. S. Schuman, W. G. Stinson, W. Chang, M. R. Hee, T. Flotte, K. Gregory, C. A. Puliafito, and J. G. Fujimoto, *Science* **254**, 1178 (1991).
28. J. G. Fujimoto, M. E. Brezinski, G. T. Tearney, S. A. Boppart, B. E. Bouma, M. R. Hee, J. F. Southern, and E. A. Swanson, *Nat. Med. (N.Y.)* **1**, 970 (1995).
29. D. C. Adler, Y. Chen, R. Huber, J. Schmitt, J. Connolly, and J. G. Fujimoto, *Nature Photon.* **1**, 709 (2007).
30. M. T. Tsai, H. C. Lee, C. K. Lee, C. H. Yu, H. M. Chen, C. P. Chiang, C. C. Chang, Y. M. Wang, and C. C. Yang, *Optics Express* **16**, 15847 (2008).
31. C. K. Lee, M. T. Tsai, H. C. Lee, Y. M. Wang, H. M. Chen, C. P. Chiang, and C. C. Yang, *J. Biomed. Opt.* **14**, 054008 (2009).
32. M. T. Tsai, C. K. Lee, H. C. Lee, H. M. Chen, C. P. Chiang, Y. M. Wang, and C. C. Yang, *J. Biomed. Opt.* **14**, 044028 (2009).
33. P. Hanarp, D. S. Sutherland, J. Gold, and B. Kasemo, *Colloids and Surfaces A: Physicochem. Eng. Aspects* **214**, 23-36 (2003).
34. E. D. Palik, *Handbook of Optical Constants of Solids* (Academic Press, Boston, 1991).
35. A. V. Belikov, K. V. Prihod'ko, O. A. Smolyanskaya, and V. A. Protasov, *J. Opt. Technol.* **70**, 811-814 (2003).

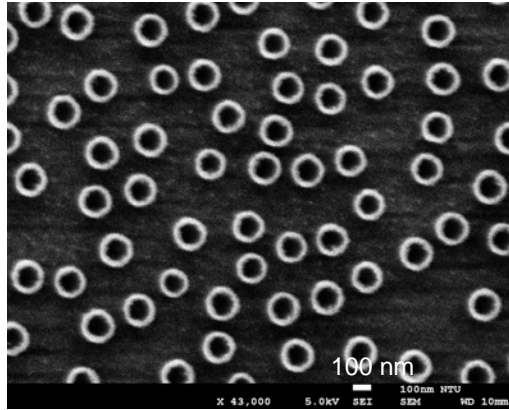


Fig. 1 Plan-view SEM image of Au NRs of sample A on a sapphire substrate

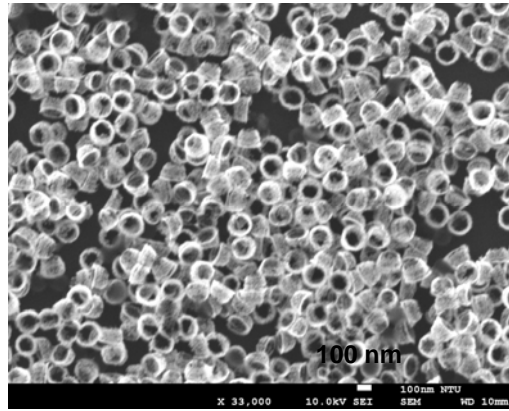


Fig. 2 Plan-view SEM image of Au NRs of sample A on a Si substrate after liftoff.

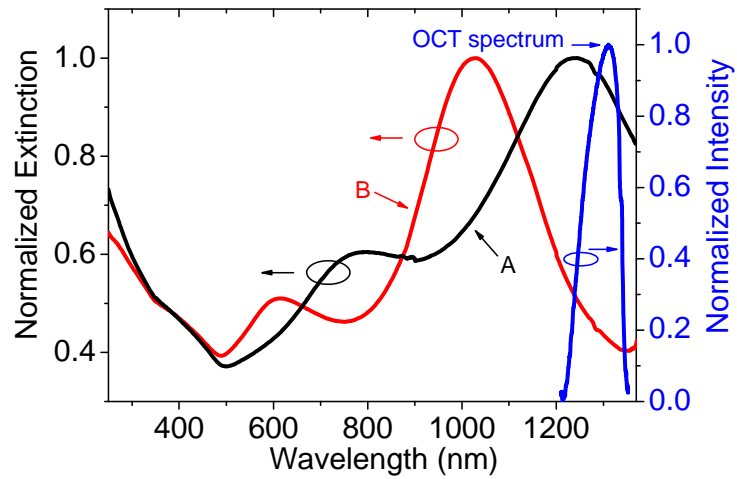


Fig. 3 Normalized extinction spectra (the left ordinate) of Au NRs measured in water solution of samples A and B. The LSP dipole resonance peaks are located at 1240 and 1030 nm for samples A and B, respectively. The light source spectrum (the right ordinate) of the used OCT system is also shown.

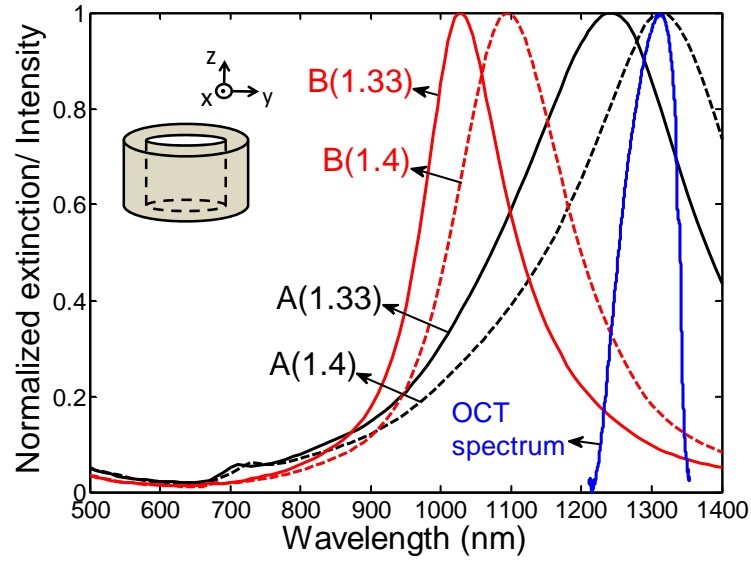


Fig. 4 Normalized extinction spectra of Au NRs of samples A and B obtained from simulations when the LSP resonance excitation light is incident along the z axis with the linear polarization in the y direction. Two sets of curves are shown for the two cases of 1.33 (in water) and 1.4 (in tissue) in refractive index (numbers shown in the parentheses of the labels). The light source spectrum of the used OCT system is also shown. The simulated NR geometry and the used coordinate system are shown in the insert.

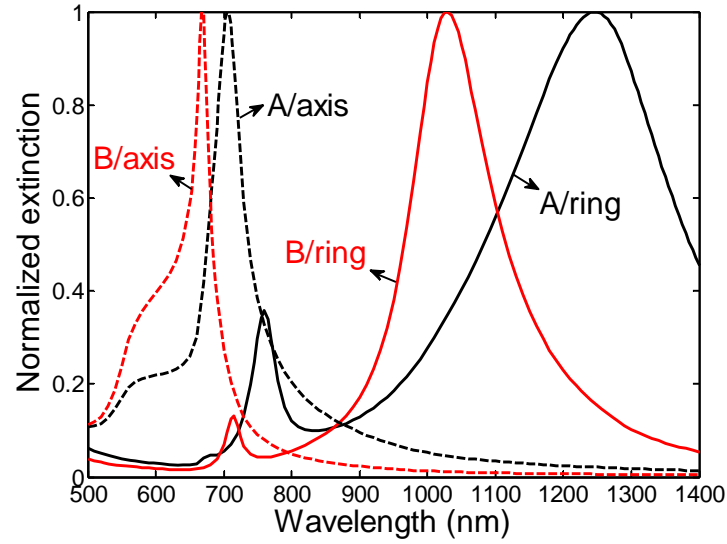


Fig. 5 Normalized extinction spectra of Au NRs of samples A and B obtained from simulations when the LSP resonance excitation light is incident in the y direction with the linear polarization along the x (for curves A/ring and B/ring) and z (for curves A/axis and B/axis) axes.

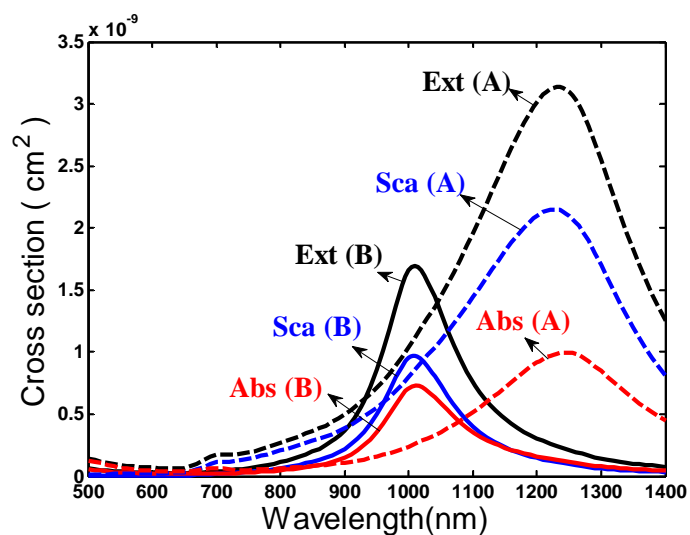


Fig. 6 Simulation results of spectral dependencies of extinction (Ext), scattering (Sca), and absorption (Abs) cross sections of a single Au NR for samples A and B.

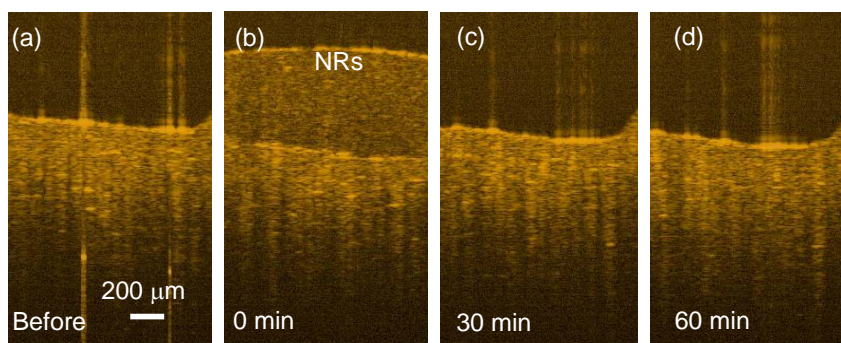


Fig. 7 OCT images of a pig adipose sample taken before (a), 0 min (b), 30 min (c), and 60 min (d) after the application of a droplet of Au NR water solution of sample B. The sample is continuously scanned with the OCT system.

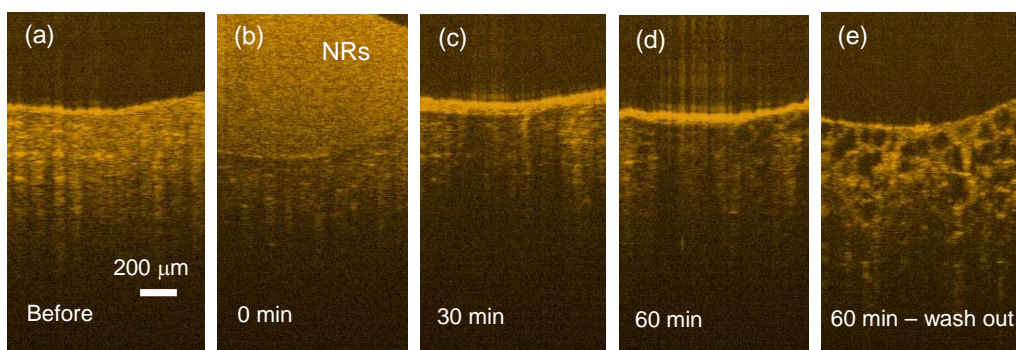


Fig. 8 OCT images of a pig adipose sample taken before (a), 0 min (b), 30 min (c), and 60 min (d) after the application of a droplet of Au NR water solution of sample A. Part (e) shows the image similar to that in part (d) after the Au NRs accumulated on the surface is washed out. The sample is continuously scanned with the OCT system.

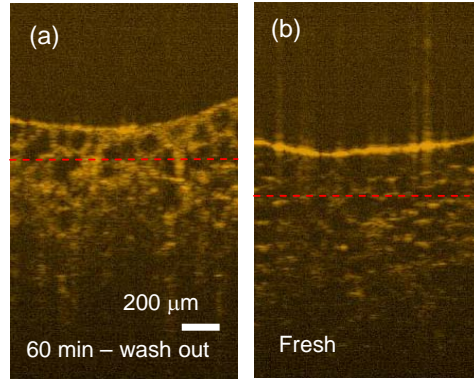


Fig. 9 OCT images of (a) a pig adipose sample with delivered resonant Au NRs (a duplicate of Fig. 8(e)) and (b) a fresh pig adipose sample (without being refrigerated or using any Au NR).

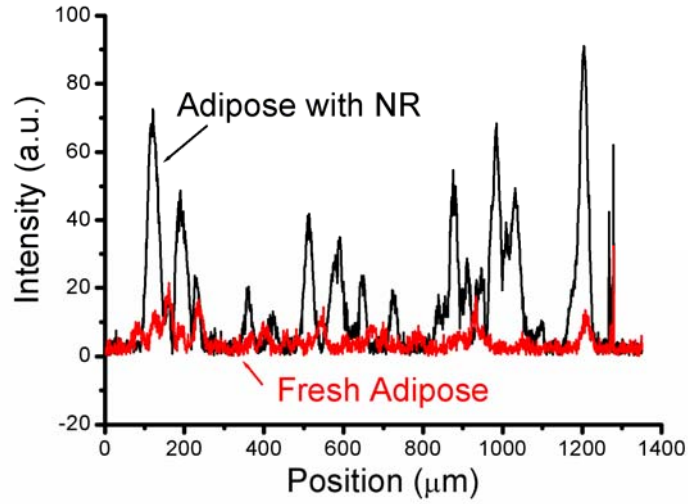


Fig. 10 OCT scan intensity distributions along the dashed lines in Figs. 9(a) (Adipose with NR) and 9(b) (Fresh Adipose).

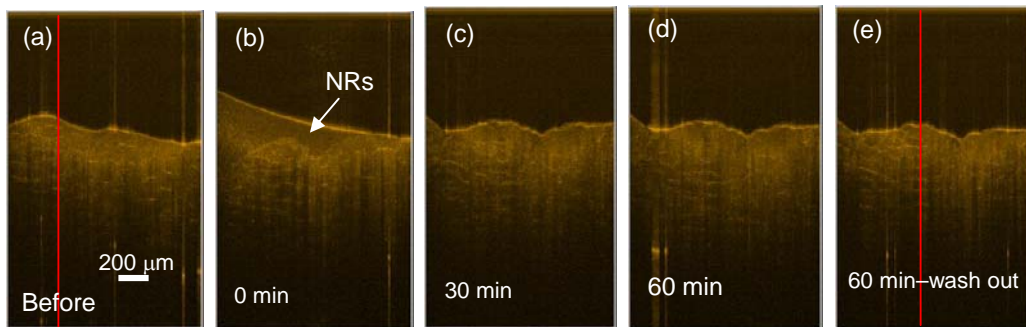


Fig. 11 OCT images of a pig adipose sample taken before (a), 0 min (b), 30 min (c), and 60 min (d) after the application of a droplet of Au NR water solution of sample A. Part (e) shows the image similar to that in part (d) after the Au NRs accumulated on the surface is washed out. The sample is scanned once every 30 min.

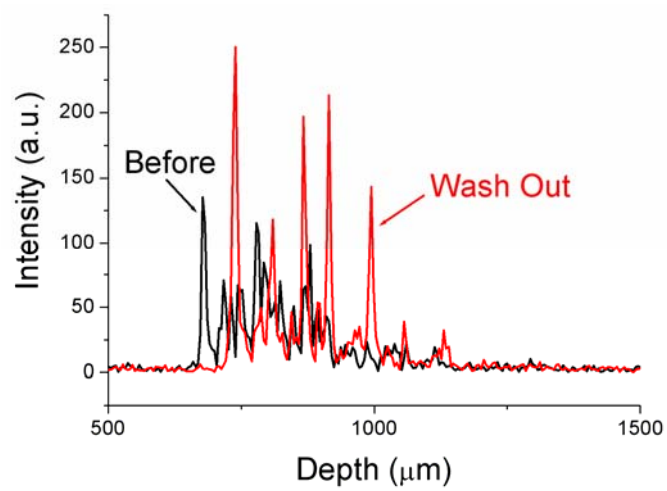


Fig. 12 OCT scan intensity distributions along the vertical lines in Figs. 11(a) (Before) and 11(e) (Wash out).

Part II: Absorption enhancement of an amorphous Si solar cell through surface plasmon-induced scattering with metal nanoparticles

1. Introduction

In an amorphous Si (a-Si) solar cell, because of the low carrier mobility, a thinner semiconductor layer has the advantage of higher carrier harvest in generating photocurrent. Also, the degradation issue in an a-Si solar cell, known as the Staebler-Wronski effect [1], requires the minimization of the active layer thickness to avoid carrier loss. However, a thin semiconductor absorbing layer may result in inefficient absorption and low device efficiency. Therefore, it is important to use certain methods for maintaining efficient absorption under the condition of a limited semiconductor thickness such that high short-circuit current and high filling factor of such a device can be achieved. Various methods for enhancing the absorption of a thin a-Si solar cell have been proposed [2-6]. Among those methods, sunlight scattering by a nanostructure, which is deposited on the top surface of a solar cell, has shown to be an effective technique. In particular, using a surface metal nanostructure for inducing surface plasmon (SP) to enhance solar cell absorption has attracted research attention in various photovoltaic materials, including organic [7-15], dye [16,17], GaAs [18,19], InGaN [20], and Si [21-30]. In each of those implementations, the absorption efficiency in a certain spectral band or the overall solar cell efficiency was more or less enhanced. The possible mechanisms of absorption enhancement with surface metal nanostructures include: 1) energy transfer from excited SPs into electrons for contributing to photovoltaic current [9]; 2) increased optical path of incident light in the absorbing layer through SP scattering [19,30]; 3) increased interaction time of light with absorbing material through SP (from ~1 to ~10 fs) [21]; 4) enhanced absorption through intense SP field [20,21,30]; and 5) enhanced light incidence into the solar cell material through the forward scattering of the metal nanostructures on the surface [22,28]. Among various metal nanostructures for the aforementioned application, the use of metal nanoparticles (NPs) for inducing localized surface plasmon (LSP) resonance represents one of the most practical approaches because of fabrication simplicity. Experimental implementations [19,23,25,26] and numerical simulations [20,23,26,29,30] have demonstrated the effectiveness and practical feasibility of this approach. However, in the previous studies of the solar cells with Au or Ag NPs on the top surfaces, significant reductions of sunlight absorption were observed in the photon energy ranges higher than the corresponding LSP resonance energies, leading to small overall increases of sunlight absorption or solar cell efficiency [18,23,29,30]. The absorption reduction originates from the sign change of the polarizability of the used metal NP, which may cause a destructive interference between the incident light and NP-scattered light in the absorption layer of the solar cell. Although the use of dielectric NP on the device top surface can avoid the destructive interference in the forward direction, the overall scattering strength is weak due to the small polarizability of a dielectric NP [28]. Therefore, searching an appropriate metal type for placing on the solar cell top surface to produce constructive interference in the forward direction and hence enhance sunlight absorption is an important issue for solar cell development. In choosing metal type for such application, one with a larger LSP resonance energy is preferred to maximize the forward constructive interference effect in the solar spectrum range. Meanwhile, since the geometry of the metal NP and its location can also effectively influence the scattering behaviors, these factors also deserve detailed investigation.

In this part of report, we demonstrate the simulation results of absorption enhancement in an a-Si solar cell by depositing metal NPs on the device top and embedding metal NPs in a layer above the Al back-reflector (back-contact). From the evaluated phase distribution results, it is found that the absorption increase is mainly caused by the enhanced near-field constructive interference effect in the forward direction through the mixture of LSP resonance and Fabry-Perot oscillation. such that an increased amount of sunlight energy is distributed in the a-Si absorption layer. The comparisons between three used metals of Al, Ag, and Au, Al NPs show the most efficient absorption enhancement, which is also larger than that of using SiO₂ NPs of the same geometry. Also, by arranging both top and bottom metal NPs in a solar cell, further absorption enhancement can be obtained. With a vertically aligned top and bottom Al nanocylinder (NC) structure, the solar cell absorption can be increased by 52 %. In section 2 of this part of report, the problem geometry and simulation method are described. The simulation results with periodical distributions of NPs on the top of a solar cell are discussed in section 3. Then, the comparisons between the cases of a periodical NP distribution and a single NP are presented in section 4. Next, the effects of adding a bottom metal NP distribution are reported in section 5. Finally, the conclusions are drawn in section 6.

2. Problem geometry and simulation method

Figures 1(a) and 1(b) show the solar cell structures used for simulation study. Except the NPs, the simulation problem geometries represent the standard structures of a-Si solar cells. Either device structure consists of (from the bottom) an Al layer as the back contact, a thin n-type a-Si layer, an intrinsic a-Si layer, a thin p-type a-Si layer, and an indium-tin-oxide (ITO) layer. The front Al contact is neglected in simulation. In the problem geometry of Fig. 1(a), which will be referred to as the case of “top NP”, a metal NP, either an NC or a nanosphere (NS), is placed at the center of the top surface in the shown simulation window. The simulation window stands for a period in the configuration of a periodical metal NP distribution in both the x and y directions. To demonstrate the LSP effect, the simulations of using SiO₂ NC and NS are also performed for comparison. In the problem geometry of Fig. 1(b), which will be referred to as the case of “double NPs”, to embed the bottom metal NP, another ITO layer is deposited between the p-type a-Si layer and the Al back contact. The NP in the bottom ITO layer contacts the bottom Al layer. To show the location of the bottom metal NP, only one-half the simulation window is shown in Fig. 1(b). The sunlight is assumed to be normally incident upon the device from the top. Although the sunlight is un-polarized, without loss of generality, we will consider polarized sunlight with the polarization oriented in the x direction. When the NPs are periodically distributed on the device surface and such a periodical arrangement does not much affect the NP scattering behaviors, or when the NPs are randomly distributed, the simulation results based on polarized sunlight can be directly applied to the real case of un-polarized sunlight due to the two-dimensionally isotropic nature of our problem; otherwise, slight modifications are needed. In Fig. 1(a), the thicknesses of the ITO, p-type a-Si, intrinsic a-Si, and n-type a-Si layers are assumed to be 20, 10, 110, and 10 nm, respectively, which represent a widely used device structure of this kind [29,30]. Here, the Al back-contact or reflector is assumed to be infinitely thick. In Fig. 1(b), the thicknesses of the top ITO, p-type a-Si, intrinsic a-Si, n-type a-Si, and bottom ITO layers are 20, 10, 100, 10, and 60 nm, respectively. The change of the thickness of the intrinsic a-Si layer from 110 into 100 nm means to optimize the absorption efficiency of the solar cell when NPs are not applied to the device. The simulation window has a dimension of 250 nm in either x or y direction. In the simulations, various metal and SiO₂ NCs and NSs of the same geometries are used. The NC has the height of 75 nm and cross-section diameter of 100 nm. The NS has the diameter of 100 nm.

The simulation computations are performed with the finite-element method (FEM). The perfectly matched layers (PMLs) are used in the +z and -z directions for simulating the infinitely extended air and Al layers. The periodic boundary conditions are imposed to the simulation window in the +x, -x, +y, and -y directions to model the problem periodicity. To investigate field scattering due to the NP, we use the well-known scattered-field formula for simulation, in which the total electromagnetic field is divided into an unperturbed part and a scattered part [31,32]. It is noted that the maximum optical intensity in the absorbing layer of the solar cell can be obtained when the unperturbed field and scattered field are in phase in the forward direction. The unperturbed field is the electromagnetic solution with the designated solar cell structure, but without the NP under the condition of an incident plane wave. It can be obtained from an explicit analytic expression. The scattering due to the NP is then described by the scattered field. In the situation with NP, the total field with the given unperturbed part in a non-PML region is governed by the two Maxwell's source-free curl equations. Because a PML serves to absorb the scattered field, in a PML region, only the scattered part needs to be described. Note that the continuity of the tangential component of the scattered field is required at the interface between a PML region and a non-PML region. Rigorously, the numerical treatment in the FEM is implemented by using the corresponding variational description [33]. In numerical computations, a commercial software (COMSOL) was used. It has provided us with a reliable framework of the aforementioned scattered-field formulation. The accuracy of our numerical results was verified through the convergence test. The minimum division mesh size was 2 nm at the metal/dielectric interface. The maximum mesh size of an individual dielectric region is set to be one tenth the shortest wavelength in material of our concern (300 nm in free space). The dielectric constant of a-Si is obtained from the measurement data in [34] except that the absorption coefficient near the band edge is corrected based on the Forouhi-Bloomer model [35]. The used refractive index and absorption coefficient as functions of wavelength for simulations are shown in Fig. 2. The dielectric constants of various metals are obtained from [34]. Fixed refractive indices of 1.46 and 1.7 are used for SiO₂ and ITO, respectively.

3. Simulation results with a periodic NP distribution on the top

Figure 3 shows the photon absorption rates as functions of wavelength with Al, Ag, Au, and SiO₂ NCs on the top of solar cells (see Fig. 1(a)). For comparison, the reference case, in which no NP is used, and the photon flux of AM 1.5G are also demonstrated. The results shown in Fig. 3 are obtained under the condition of periodical NP distributions with the period of 250 nm in both x and y directions. Here, one can see the oscillatory behavior of the reference curve due to the Fabry-Perot effect in the vertical direction. When an Au or Ag NC is placed on the top, the photon absorption in the UV-blue-green range is essentially reduced. However, on the long-wavelength side, absorption is enhanced except in the range between 690 and 800 nm, in which a Fabry-Perot peak in the reference case becomes weakened when a metal NC is used. As a result, the integrated photon absorption rate in the case of Au (Ag) NC is reduced (enhanced) by 9 (10) %, when compared with the reference case. The integrated photon absorption rates under various conditions are listed in Table I. In Fig. 3, one can also see that when an Al NC is placed on the device top, the photon absorption rate is always enhanced in the whole concerned spectral range except that between 690 and 800 nm, leading to the increase of integrated photon absorption rate by 39 %. For comparison, a SiO₂ NC of the same geometry is also used for evaluating the photon absorption rate. In this situation, the photon absorption rate is also significantly increased (by 16 %), as compared with the reference case. Because the absorption layer of the solar cell is below the NP by 20-150 nm, the absorption enhancement is supposed to be due to the enhanced near-field constructive interference effect of sunlight in the absorption layer. The interference behavior is controlled by the relative phase between the aforementioned unperturbed and scattered fields. The phase differences between the unperturbed and scattered fields at the location right below the NP center with a depth of 65 nm from the top surface of the p-type a-Si layer as functions of wavelength for the four kinds of NP are shown in Fig. 4. Here, one can see that among the metal NPs, the phase difference of the Al case is generally smaller than those of the Au and Ag cases. However, the phase difference of the SiO₂ case is generally the smallest among the four cases. The non-zero phase difference in the SiO₂ case is mainly due to the layered structure of the solar cell. The deviations of the phase difference curves from the SiO₂ case in using metal NPs are strongly related to LSP resonances. According to the Mie theory [36], the phase distribution of the perturbed field behind a metal NP is usually significantly altered. However, because of the complex solar cell structure, the spectral distributions of phase difference become complicated even though the extinction spectral peaks of the Al, Ag, and Au NP cases can be identified to be at 420, 570, and 640 nm, respectively. These wavelengths are marked by the vertical arrows in Fig. 4. It is noted that all the four curves in Fig. 4 have peaks around 660 nm. Also, the three metal curves have a common dip around 720 nm, which is shifted to ~740 nm in the SiO₂ curve. The peaks and dips correspond to Fabry-Perot resonance and anti-resonance spectral positions, respectively, which have been influenced by the NP. Here, the common Fabry-Perot behaviors lead to the similar spectral features beyond 630 nm in wavelength. It is noted that by using a SiO₂ NP, although the optical intensity in the forward direction can be relatively stronger when compared with those in other directions, its overall scattering is not as strong as that of an Al NP, which has the LSP resonance effects, such that its absorption enhancement is smaller than that of the Al NP case.

The results in Figs. 3 and 4 show the superiority of using Al NC for increasing absorption through the enhancement of the constructive interference effect in the forward direction. To understand the effects of NP geometry, we repeat the simulation for Fig. 3 by replacing NCs by NSs. The results similar to Fig. 3 are shown in Fig. 5. Here, one can see that SiO₂ NS also significantly enhances photon absorption rate (also by 16 % when compared with the reference case, as shown in Table I). Al NS still leads to the largest absorption enhancement. By using Al (Ag) NSs, the photon absorption rate can be increased by 31 (22) %, when compared with the reference case (see Table I). Also, Au NS results in slight absorption enhancement (by 3 %). In the Ag and Au cases, the use of NS results in increased enhancements; however, in the Al case, the use of NS leads to reduced enhancement, when compared with the individual cases of NC. Figure 6 shows the phase difference data similar to those in Fig. 4 for the cases of NS. Here, one can see the similar behaviors to those shown in Fig. 4. The SiO₂ case has generally the smallest phase difference between the unperturbed and scattered light, followed by the Al case. The three wavelengths for the maximum extinctions (LSP resonances) at 310, 415, and 550 nm of the Al, Ag, and Au cases, respectively, are also marked by vertical arrows in Fig. 6. The significantly shorter wavelengths for LSP resonances in the cases of NS are attributed to the much smaller contact area of an NS with the device surface. The LSP resonances in the NC cases are strongly influenced by the contacting ITO layer. It is noted that both SiO₂ curves

in Figs. 4 and 6 show a common peak near 480 nm, around which the curves of metal NCs and NSs also show local maxima. This feature can be caused by the interference behavior of the multi-layer solar cell structure and is common in all cases. In the Al case, because of the end-facet contact of an NC with the top ITO of 1.7 in refractive index, the resonance wavelength of the dominant substrate LSP mode [32] is located at 420 nm (see Fig. 4). At this wavelength, the LSP-induced absorption enhancement is more prominent due to stronger sunlight intensity, when compared with the case of Al NS, in which the surrounding air results in the LSP resonance wavelength around 310 nm (see Fig. 6) of weak sunlight intensity. Therefore, an Al NC leads to a higher absorption enhancement than an Al NS. On the other hand, in the cases of Ag and Au, the LSP resonances with both NC and NS are located in the spectral range of high sunlight intensity. However, because of the sharp metal edges, which cause higher Ohmic loss, in the NC geometry, the relatively higher dissipation in Ag and Au (compared with Al) results in higher loss in the NC geometry, when compared with the NS geometry. Hence, the absorption enhancements in the Ag and Au NC cases become lower than those in the corresponding NS cases.

To further understand the enhanced constructive interference effect in the forward direction, the distributions of electrical intensity enhancement ratios with respect to the reference case for the total field within the a-Si regions in the x-z plane are shown in Fig. 7. Here, $x = 0$ corresponds to the center of the NP. Also, $z = 0$ corresponds to the bottom of the n-type a-Si layer. The two horizontal white dashed lines represent the boundaries between the p-type and intrinsic a-Si layers and between the intrinsic and n-type layers. Figures 7(a)-7(h) correspond to the cases of Al NC at 525 nm (enhanced), Ag NC at 600 nm (enhanced), Ag NC at 405 nm (suppressed), SiO₂ NC at 525 nm (enhanced), Al NS at 525 nm (enhanced), Ag NS at 525 nm (enhanced), Ag NS at 405 nm (suppressed), and SiO₂ NS at 525 nm (enhanced), respectively. Here, one can see from Figs. 7(c) and 7(g) that the reduction trend of the constructive interference effect significantly decreases sunlight absorption of the whole a-Si layer. The formation of the two bright spots in the situations of strong constructive interference effect is attributed to Fabry-Perot oscillation. It is noted that the color coding scales are different among different cases in Fig. 7. By comparing the group of Figs. 7(a) and 7(e) with the group of Figs. 7(d) and 7(h), one can see that the scattering strength of a SiO₂ NP is indeed lower than that of an Al NP, leading to the relatively smaller absorption enhancement in the case of SiO₂ NP.

4. Simulation results with a single NP on the top

The results given above correspond to the condition of periodic NP distribution on the device top. In this section, we show the solar cell absorption behaviors when a single metal NP is used. Figure 8 shows the comparisons of photon absorption rate as a function of wavelength between the cases of single NC and periodic NC distributions of Al, Ag, and Au. Again, the curves of reference and AM 1.5G are also depicted for comparison. To obtain the data in Fig. 8, we assume that the effective absorption region, which is defined for evaluating the total photon absorption rate, is a circular area of 282 nm in diameter. The assumption of this diameter value means to make the effective absorption area the same as that (250 nm x 250 nm) in the cases of periodical NP distributions. Here, one can see that the spectral oscillation patterns of photon absorption rate are different between the cases of single NC and periodic NC distribution. The periodic distribution of NC leads to certain diffraction effects and changes the local Fabry-Perot behaviors. Also, the LSP interaction between neighboring NPs may also cause the changes of spectral patterns. One can observe alternative variations of enhancement and suppression with wavelength in comparing the cases of single NC and periodic NC distribution. The integrated photon absorption rates and their ratios with respect to the reference level are listed in Table II. Here, one can see the slight increase of photon absorption rate by using a single NP of any concerned metal, when compared with the condition of periodical NP distribution.

Figures 9(a) and 9(b) show the distributions of electric intensity enhancement ratios over that of the reference case at 500 nm in wavelength in the x-y plane at the depth of 65 nm from the top surface of the p-a-Si layer with the circles centered at the centers an Al NC (a) and an Ag NC (b) of 100 nm in diameter on the device top. The values of D in nm indicate the diameters of the white dashed circular curves. Here, one can see the enhanced and reduced intensity distributions right below the Al and Ag NC, respectively. The total photon absorption rates shown in Fig. 8 depend on the definition of the effective absorption area. Figure 10 shows the enhancement ratios of photon absorption as functions of the effective absorption diameter. The enhancement ratio is defined as the ratio of the integrated photon absorption rate in the case with NC over that without NC (the reference). Therefore, in Fig. 10, when the effective absorption diameter approaches infinity, the enhancement ratio will asymptotically

approach one. Here, one can see that by using an Au NC, when the effective absorption diameter is between 200 and 500 nm, the enhancement ratio is always smaller than unity, implying that in this situation the incident sunlight is either absorbed by the Au NP, backscattered into air, or scattered in a manner that the photon energy is pushed away from the designated effective absorption region. On the other hand, by using an Al or Ag NC, the enhancement ratio decreases monotonically with effective absorption diameter. In particular, the use of an Ag NC leads to a faster decay into unity, implying that the effect of Ag NC scattering is limited to a smaller region around the metal NP when compared with that of Al NC scattering. By using an Al or Ag NC, the metal NP can “attract” sunlight energy into the designated effective absorption region from outside.

5. Comparison between the cases of top, bottom, and double NPs

The results above show the enhanced constructive interference effects in the forward direction by placing metal and dielectric NPs on the front (top) side of a solar cell. In this section, we demonstrate the effects of enhanced backscattering by depositing metal NPs on the backside (bottom side) of the solar cell. For this purpose, we consider the device structure shown in Fig. 1(b). To embed a metal NP between the Al back-contact and the n-a-Si layer, an ITO layer is inserted in between. Here, we assume that an Al NC is embedded in this ITO layer. For our simulations, we also assume that the bottom Al NC has a diameter of 100 nm and a height of 60 nm (smaller than that of the top metal NC at 75 nm). This NC height is the same as the thickness of the bottom ITO layer such that the bottom metal NC contacts with both the n-a-Si layer above and the Al back-contact below. In this solar cell, the thickness of the i-a-Si layer is reduced from 110 nm to 100 nm to optimize the Fabry-Perot oscillation for maximizing the absorption in the reference case. Figure 11 shows the photon absorption rates as functions of wavelength in the cases of periodical top Al NC distribution (top), periodical bottom Al NC distribution (bottom), and both top and bottom Al NC distributions (double). In the case of double NCs, the top and bottom Al NCs are vertically aligned (the same x-y coordinates). The curves of the reference case (no metal NP) and AM 1.5G are also shown for comparison. Here, one can see that without the top Al NC, the use of the bottom Al NC suppresses the absorption near its peak around 525 nm. However, two absorption peaks are formed around 675 and 750 nm by using the bottom Al NC for enhancing the integrated absorption. These two peaks correspond to the LSP resonances of the bottom Al NC. However, the formation of these peaks results in only 10 % increase of integrated absorption, which is significantly lower than the 39 % absorption enhancement in the case of top Al NC only, as shown in Table III. Nevertheless, the combination of the vertically aligned top and bottom Al NCs can lead to an integrated absorption enhancement of 52 %. Compared with the case of top Al NC only, the addition of the bottom Al NC results in a significant absorption increase on the long-wavelength side even though that around the peak is slightly reduced. In this situation, the integrated absorption is significantly enhanced. Figures 12(a)-12(i) show the distributions of electrical intensity enhancement ratios (over that of the reference case) in the x-z plane of the cases in Fig. 11 with (a)-(c) for the cases of top NC, (d)-(f) for the cases of bottom NC, and (g)-(i) for the cases of double NCs. The corresponding wavelengths are 525 nm in (a), (d), and (g), 600 nm in (b), (e), and (h), and 675 nm in (c), (f), and (i). The two horizontal white dashed lines represent the boundaries between the p-type and intrinsic a-Si layers and between the intrinsic and n-type layers. Here, one can see that at each wavelength, the intensity enhancement patterns are similar among the cases of top NC, bottom NC, and double NCs, except that in Fig. 12(c). However, the levels of enhancement are quite different. The significantly higher enhancement levels in the case of double NCs can be clearly seen.

In Figs. 11 and 12, we demonstrate the absorption enhancement when the top and bottom Al NCs are vertically aligned. In Figs. 13 and 14, we compare the results of different misalignments between the top and bottom Al NCs. Figure 13 shows the photon absorption rates as functions of wavelength in various cases of double Al NCs with the vertical alignment shifted horizontally by one-quarter ($\Lambda/4$ shift) and one-half ($\Lambda/2$ shift) the period, Λ , in the x- and y directions. The incident sunlight is assumed to be x-polarized. The curves of no shift, reference, and AM 1.5G are also shown for comparison. Here, one can see that the misalignments cause minor modifications of the absorption curves. Clear changes are observed at the kinks around 600 nm. This feature can be due to the Fabry-Perot effect between the top and bottom NCs when they are vertically aligned. As the two NCs become misaligned, this kink becomes less prominent. The integrated photon absorption rates and their ratios with respect to the reference level of various cases are shown in Table III. Here, one can see that with even up to one-half period misalignments, the integrated photon absorption rates are only slightly reduced (by up to 6 %). Therefore, the vertical alignment of the top and bottom NCs is not

critical for enhancing absorption under the assumed condition of periodical NC distributions at the top and bottom. Figures 14(a)-14(l) show the distributions of electrical intensity enhancement ratios (over that of the reference case) in the x-z plane of the cases in Fig. 13 with (a)-(c) for the case of $\Lambda/4$ shift-x, (d)-(f) for the case of $\Lambda/2$ shift-x, (g)-(i) for the case of $\Lambda/4$ shift-y, and (j)-(l) for the case of $\Lambda/2$ shift-y. The corresponding wavelengths are 525 nm in (a), (d), (g), and (j), 600 nm in (b), (e), (h), and (k), and 675 nm in (c), (f), (i), and (l). The two horizontal white dashed lines represent the boundaries between the p-type and intrinsic a-Si layers and between the intrinsic and n-type layers. It is noted that Figs. 14(g)-14(l), which demonstrate the intensity enhancement ratio distributions in the x-z plane by shifting the alignments in the y direction, look similar to Figs. 12(g)-12(i). Because of the symmetrical NC arrangements between the x and y axes, the misalignments in the y direction does not seem to affect much the electrical intensity distributions. However, it is worth mentioning that the slight changes, particularly in Fig. 14(j), can be attributed to the misalignment in the other direction and the oriented incident polarization (in the x direction). Regarding the results in Figs. 14(a)-14(f), we can first notice the horizontal shifts of the bright spots in Figs. 14(c) and 14(f) (at 675 nm in wavelength) from the center, as the cases shown in Figs 14(i) and 14(l), by 62.5 and 125 nm, which correspond to $\Lambda/4$ and $\Lambda/2$ shifts, respectively. As mentioned earlier, the feature around 675 nm in Figs. 11 and 13 is due to the LSP resonance of the bottom Al NC. The location of resonance field distribution shifts with the NC position. The bright spots in Figs. 14(b) and 14(e) (at 600 nm in wavelength) also show horizontal shifts with respect to those in Figs. 14(h) and 14(k). However, the shift ranges are significantly smaller than the corresponding misalignment ranges, $\Lambda/4$ and $\Lambda/2$, respectively. As pointed out earlier, the feature around 600 nm is related to the Fabry-Perot effect between the top and bottom Al NCs. Therefore, although they are separated by $\Lambda/4$ or $\Lambda/2$, the maximum intensity locations (the bright spots) in between do not shift that much in the x direction. Then, at 525 nm in wavelength, such interactions between the top and bottom Al NCs are stronger such that the horizontal shift ranges of the lower bright spots become even smaller, as shown in Figs. 14(a) and 14(d), when compared with those in Figs. 14(g) and 14(j). The detailed interactions between the top and bottom metal NPs, including the Fabry-Perot effect and the possible LSP coupling, deserve further investigation.

6. Conclusions

In summary, we have demonstrated the simulation results of absorption enhancement in an a-Si solar cell by depositing metal NPs on the device top and embedding metal NPs in a layer above the Al back-reflector. The absorption increase resulted from the near-field constructive interference of optical fields in the forward direction such that an increased amount of sunlight energy was distributed in the a-Si absorption layer. Among the three used metals of Al, Ag, and Au, Al NP showed the most efficient absorption enhancement. Between the two used NP geometries, Al NCs were more effective in absorption enhancement than Al NSs. Also, a random distribution of isolated NCs could lead to higher absorption enhancement, when compared with the cases of periodical NC distributions. Meanwhile, the fabrications of both top and bottom Al NCs in a solar cell resulted in further absorption enhancement. Misalignments between the top and bottom Al NCs did not significantly reduce the enhancement percentage. With a vertically aligned top and bottom Al NC structure, the solar cell absorption could be increased by 52 %.

References:

1. D. L. Staebler and C. R. Wronski, "Reversible conductivity changes in discharge-produced amorphous Si," *Appl. Phys. Lett.* **31**, 292-294 (1977).
2. L. Zeng, P. Bermel, Y. Yi, B. A. Alamariu, K. A. Broderick, J. Liu, C. Hong, X. Duan, J. Joannopoulos, and L. C. Kimerling, "Demonstration of enhanced absorption in thin film Si solar cells with textured photonic crystal back reflector," *Appl. Phys. Lett.* **93**, 221105 (2008).
3. P. Bermel, C. Luo, L. Zeng, L. Kimerling, and J. D. Joannopoulos, "Improving thin-film crystalline silicon solar cell efficiencies with photonic crystals," *Opt. Express* **15**, 16986-17000 (2007).
4. A. Poruba, A. Fejfar, Z. Remes, J. Springer, M. Vanecsek, J. Kocka, J. Meier, P. Torres, and A. Shah "Optical absorption and light scattering in microcrystalline silicon thin films and solar cells," *J. Appl. Phys.* **88**, 148-160 (2000).
5. M. A. Green, "Lambertian light trapping in textured solar cells and light-emitting diodes: Analytical solutions," *Prog. Photovolt: Res. Appl.* **10**, 235-241 (2002).

6. S. Fahr, C. Rockstuhl, and F. Lederer, "Engineering the randomness for enhanced absorption in solar cells," *Appl. Phys. Lett.* **92**, 171114 (2008).
7. T. Kume, S. Hayashi and K. Yamamoto, "Enhancement of photoelectric conversion efficiency in copper phthalocyanine solar cell by surface plasmon excitation," *Jpn. J. Appl. Phys.* **32**, 3486-3492 (1993).
8. T. Kume, S. Hayashi, H. Ohkuma, K. Yamamoto "Enhancement of photoelectric conversion efficiency in copper phthalocyanine solar cell: white light excitation of surface plasmon polaritons," *Jpn. J. Appl. Phys.* **34**, 6448-6451 (1995).
9. M. Westphalen, U. Kreibig, J. Rostalski, H. Lüth, and D. Meissner, "Metal cluster enhanced organic solar cells," *Solar Energy Materials and Solar Cells* **61**, 97-105 (2000).
10. M. Niggemann, M. Glatthaar, A. Gombert, A. Hinsch, and V. Wittwer, "Diffraction gratings and buried nano-electrodes—architectures for organic solar cells," *Thin Solid Films* **451-452**, 619-624 (2004).
11. B. P. Rand, P. Peumans, and S. R. Forrest, "Long-range absorption enhancement in organic tandem thin-film solar cells containing silver nanoclusters," *J. Appl. Phys.* **96**, 7519-7526 (2004).
12. K. Tvingstedt, N. Persson, O. Inganäs, A. Rahachou, and I. V. Zozoulenko, "Surface plasmon increase absorption in polymer photovoltaic cells," *Appl. Phys. Lett.* **91**, 113514 (2007).
13. A. J. Morfa, K. L. Rowlen, T. H. Reilly, III, M. J. Romero, and J. van de Lagemaat, "Plasmon-enhanced solar energy conversion in organic bulk heterojunction photovoltaics," *Appl. Phys. Lett.* **92**, 013504 (2008).
14. S. S. Kim, S. I. Na, J. Jo, D. Y. Kim, and Y. C. Nah, "Plasmon enhanced performance of organic solar cells using electrodeposited Ag nanoparticles," *Appl. Phys. Lett.* **93**, 073307 (2008).
15. X. Chen, C. Zhao, L. Rothberg, and M. K. Ng, "Plasmon enhancement of bulk heterojunction organic photovoltaic devices by electrode modification," *Appl. Phys. Lett.* **93**, 123302 (2008).
16. K. Kato, H. Tsuruta, T. Ebe, K. Shinbo, F. Kaneko, and T. Wakamatsu, "Enhancement of optical absorption and photocurrents in solar cells of merocyanine Langmuir–Blodgett films utilizing surface plasmon excitations," *Materials Science and Engineering C* **22**, 251-256 (2002).
17. C. Hägglund, M. Zäch, and B. Kasemo, "Enhanced charge carrier generation in dye sensitized solar cells by nanoparticle plasmons," *Appl. Phys. Lett.* **92**, 013113 (2008).
18. K. Nakayama, K. Tanabe, and H. A. Atwater, "Plasmonic nanoparticle enhanced light absorption in GaAs solar cells," *Appl. Phys. Lett.* **93**, 121904 (2008).
19. V. E. Ferry, L. A. Sweatlock, D. Pacifici, and H. A. Atwater, "Plasmonic nanostructure design for efficient light coupling into solar cells," *Nano Lett.* **8**, 4391-4397 (2008).
20. J. Y. Wang, F. J. Tsai, J. J. Huang, C. Y. Chen, N. Li, Y. W. Kiang, and C. C. Yang, "Enhancing InGaN-based solar cell efficiency through localized surface plasmon interaction by embedding Ag nanoparticles in the absorbing layer," *Opt. Express* **18**, 2682-2694 (2010).
<http://www.opticsinfobase.org/oe/abstract.cfm?URI=oe-18-3-2682>
21. D. M. Schaadt, B. Feng, and E. T. Yu, "Enhanced semiconductor optical absorption via surface plasmon excitation in metal nanoparticles," *Appl. Phys. Lett.* **86**, 063106 (2005).
22. D. Derkacs, S. H. Lim, P. Matheu, W. Mar, and E. T. Yu, "Improved performance of amorphous silicon solar cells via scattering from surface plasmon polaritons in nearby metallic nanoparticles," *Appl. Phys. Lett.* **89**, 093103 (2006).
23. S. H. Lim, W. Mar, P. Matheu, D. Derkacs, and E. T. Yu, "Photocurrent spectroscopy of optical absorption enhancement in silicon photodiodes via scattering from surface plasmon polaritons in gold nanoparticles," *J. Appl. Phys.* **101**, 104309 (2007).
24. K. R. Catchpole and S. Pillai, "Surface plasmons for enhanced silicon light-emitting diodes and solar cells," *J. Luminescence* **121**, 315-318 (2006).
25. S. Pillai, K. R. Catchpole, T. Trupke, and M. A. Green, "Surface plasmon enhanced silicon solar cells," *J. Appl. Phys.* **101**, 093105 (2007).
26. C. Hägglund, M. Zäch, G. Petersson, and B. Kasemo, "Electromagnetic coupling of light into a silicon solar cell by nanodisk plasmons," *Appl. Phys. Lett.* **92**, 053110 (2008).
27. F. -J. Haug, T. Söderström, O. Cubero, V. Terrazzoni-Daudrix, and C. Ballif, "Plasmonic absorption in textured silver back reflectors of thin film solar cells," *J. Appl. Phys. Lett.* **104**, 064509 (2008).
28. P. Matheu, S. H. Lim, D. Derkacs, C. McPheeters, and E. T. Yu, "Metal and dielectric nanoparticle scattering for improved optical absorption in photovoltaic devices," *Appl. Phys. Lett.* **93**, 113108 (2008).

29. C. Rockstuhl and F. Lederer, "Photon management by metallic nanodiscs in thin film solar cells," *Appl. Phys. Lett.* **94**, 213102 (2009).
30. C. Rockstuhl, S. Fahr, and F. Lederer, "Absorption enhancement in solar cells by localized plasmon polaritons," *J. Appl. Phys.* **104**, 123102 (2008).
31. A. Kirsch and P. Monk, "A finite element method for approximating electromagnetic scattering from a conducting object," *Numer. Math.* **92**, 501–534 (2002).
32. C. Y. Chen, J. Y. Wang, F. J. Tsai, Y. C. Lu, Y. W. Kiang, and C. C. Yang, "Fabrication of sphere-like Au nanoparticles on substrate with laser irradiation and their polarized localized surface plasmon behaviors," *Opt. Express* **17**, 14186–14198 (2009).
33. J. Jin and D. J. Riley, *Finite Element Analysis of Antennas and Arrays* (John Wiley & Sons, Inc., New Jersey, 2009).
34. E. D. Palik, *Handbook of Optical Constants of Solids* (Academic Press, Boston, 1991).
35. A. R. Forouhi and I. Bloomer, "Optical dispersion relations for amorphous semiconductors and amorphous dielectrics," *Phys. Rev. B* **34**, 7018–7026 (1986).
36. S. A. Maier, *Plasmonics: Fundamentals and Applications* (Springer, New York, 2007).

Table I Integrated photon absorption rates and their ratios with respect to the reference level of various cases in Figs. 3 and 5. The photon absorption rate of AM 1.5G covers the whole solar spectral range.

AM 1.5G	Reference	Al NC	Ag NC	Au NC	SiO ₂ NC	Al NS	Ag NS	Au NS	SiO ₂ NS
25.6*	$3.36 \times 10^7 \text{ s}^{-1}$	4.68*	3.68*	3.05*	3.89*	4.40*	4.11*	3.45*	3.90*
ratio	1	1.39	1.10	0.91	1.16	1.31	1.22	1.03	1.16

* $\times 10^7 \text{ s}^{-1}$

Table II Integrated photon absorption rates and their ratios with respect to the reference level of various cases in Fig. 8. The photon absorption rate of AM 1.5G covers the whole solar spectral range.

AM 1.5G	Reference	Single Al	Periodic Al	Single Ag	Periodic Ag	Single Au	Periodic Au
25.6*	$3.36 \times 10^7 \text{ s}^{-1}$	4.76*	4.68*	3.84*	3.68*	3.10*	3.05*
ratio	1	1.42	1.39	1.14	1.10	0.92	0.91

* $\times 10^7 \text{ s}^{-1}$

Table III Integrated photon absorption rates and their ratios with respect to the reference level of various cases in Figs. 11 and 12. The photon absorption rate of AM 1.5G covers the whole solar spectral range.

AM 1.5G	Reference	Top NC	Bottom NC	Double NCs or no shift	$\Lambda/4$ shift-x	$\Lambda/2$ shift-x	$\Lambda/4$ shift-y	$\Lambda/2$ shift-y
25.6*	$3.38 \times 10^7 \text{ s}^{-1}$	4.68*	3.71*	5.13*	5.04*	4.97*	5.04*	4.93*
ratio	1	1.39	1.10	1.52	1.49	1.47	1.49	1.46

* $\times 10^7 \text{ s}^{-1}$

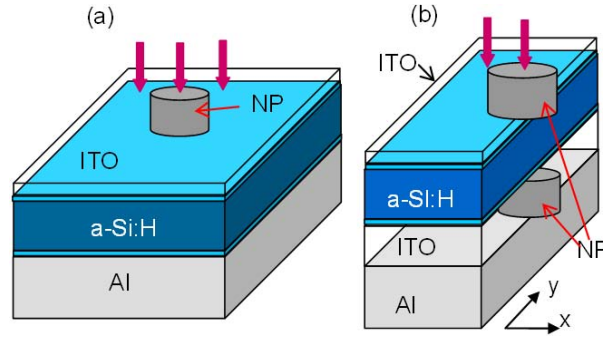


Fig. 1 (a) Solar cell structure in a simulation window with an NP on the top; (b) Solar cell structure in one-half the simulation window with a metal NP on the top and another metal NP in the bottom ITO layer contacting the bottom Al layer.

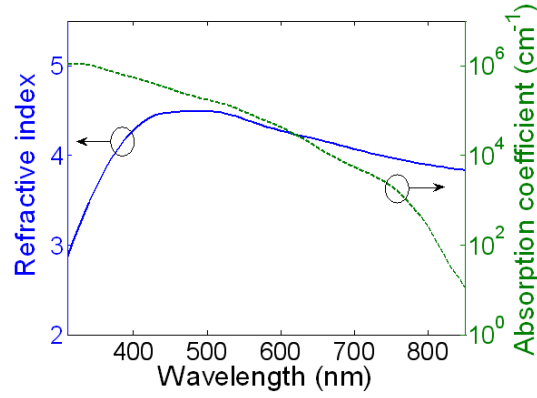


Fig. 2 Used refractive index and absorption coefficient of a-Si for simulations obtained from Refs. 34 and 35.

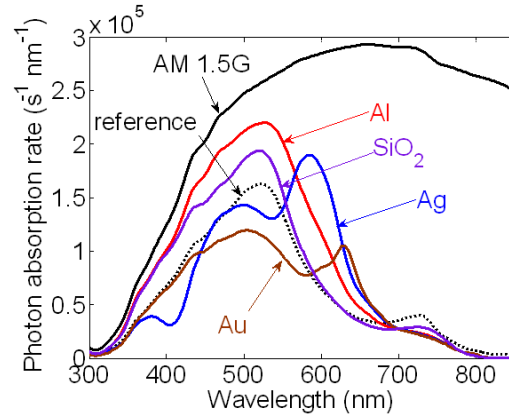


Fig. 3 Photon absorption rates as functions of wavelength with Al, Ag, Au, and SiO₂ NCs on the top of a solar cell. For comparison, the reference case, in which no NP is used, and the photon flux of AM 1.5G are also demonstrated.

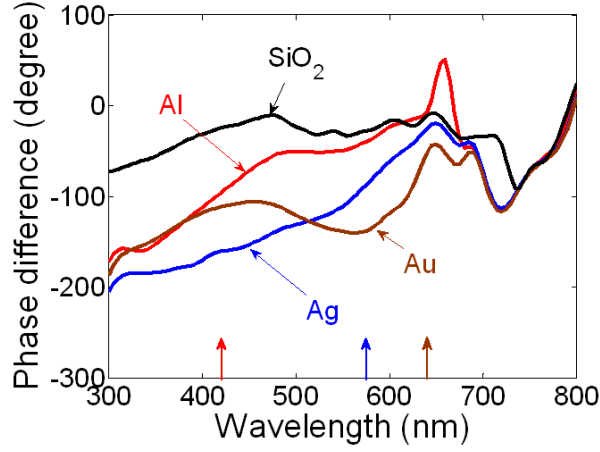


Fig. 4 Phase differences as functions of wavelength between the unperturbed and scattered fields when Al, Ag, Au, and SiO_2 NCs are used in the solar cell structure shown in Fig. 1(a).

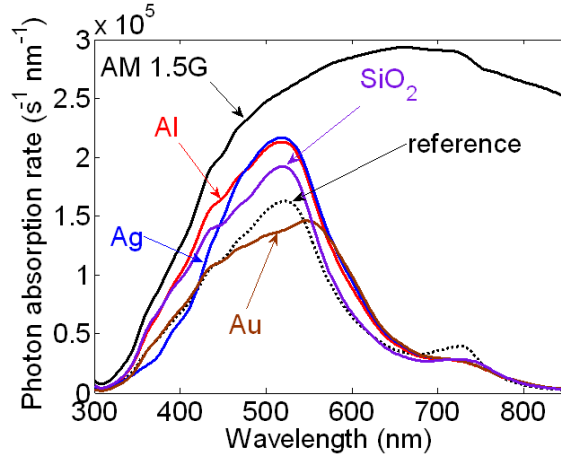


Fig. 5 Photon absorption rates as functions of wavelength with Al, Ag, Au, and SiO_2 NSs on the top of solar cells. For comparison, the reference case, in which no NP is used, and the photon flux of AM 1.5G are also demonstrated.

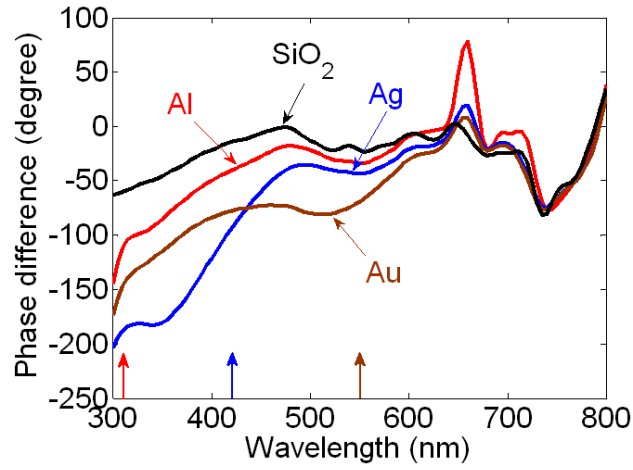


Fig. 6 Phase differences as functions of wavelength between the unperturbed and scattered fields when Al, Ag, Au, and SiO_2 NSs are used in the solar cell structure shown in Fig. 1(a).

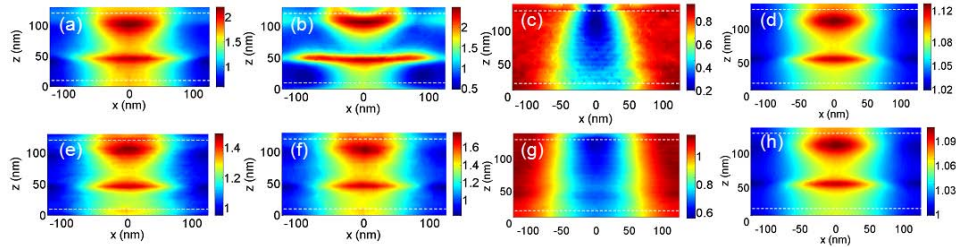


Fig. 7 Distributions of electrical intensity enhancement ratios (over that of the reference case) within the a-Si regions in the x-z plane. Here, $x = 0$ corresponds to the center of the NP. The two horizontal white dashed lines represent the boundaries between the p-type and intrinsic a-Si layers and between the intrinsic and n-type layers. Parts (a)-(h) correspond to the cases of Al NC at 525 nm (enhanced), Ag NC at 600 nm (enhanced), Ag NC at 405 nm (suppressed), SiO₂ NC at 525 nm (enhanced), Al NS at 525 nm (enhanced), Ag NS at 525 nm (enhanced), Ag NS at 405 nm (suppressed), and SiO₂ NS at 525 nm (enhanced), respectively.

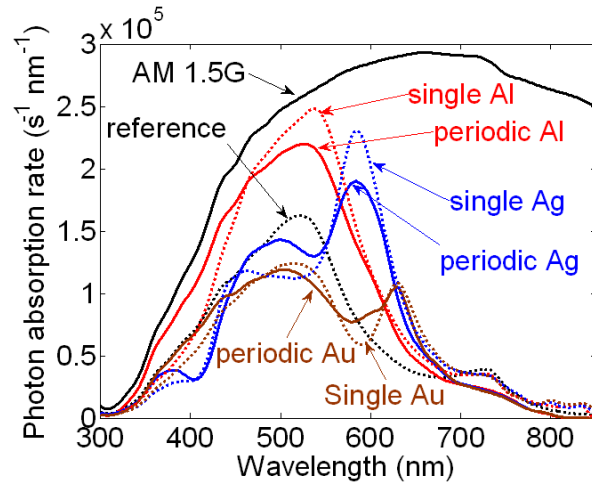


Fig. 8 Comparisons of photon absorption rate between the cases of periodical top metal NC distributions (curves of periodic Al, periodic Ag, and periodic Au) and single top metal NP configurations (curves of single Al, single Ag, and single Au). The curves of reference (no NP) and photon flux of AM 1.5G are also shown for comparison.

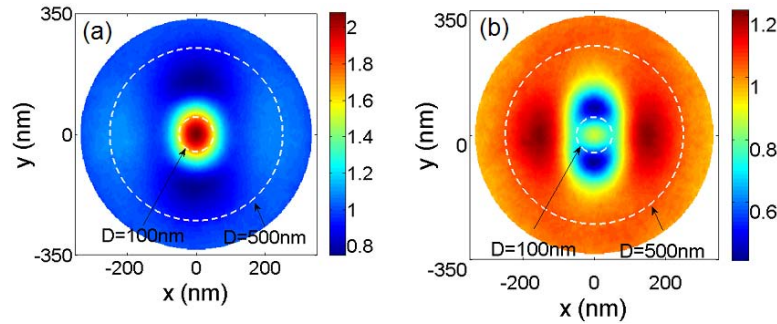


Fig. 9 Distributions of electrical intensity enhancement ratios (over that of the reference case) at 500 nm in wavelength in the x-y plane at the depth of 65 nm from the top surface of the p-a-Si layer with the circles centered at the centers of an Al NC (a) and an Ag NC (b) of 100 nm in diameter on the device top. The values of D in nm indicate the diameters of the white dashed circular curves.

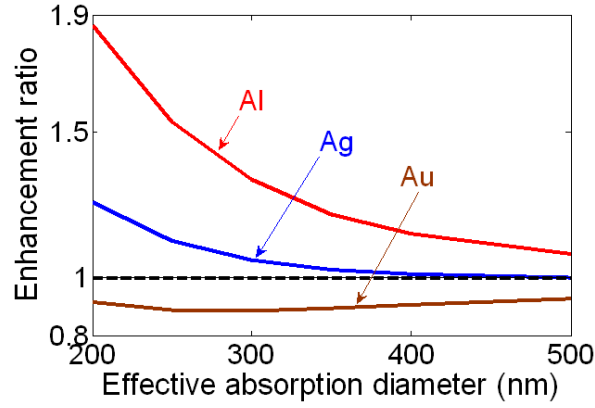


Fig. 10 Enhancement ratios as functions of effective absorption diameter with respect to the reference case when single Al, Ag, and Au NCs are individually placed at the device top, corresponding to the data in Figs. 8 and 9.

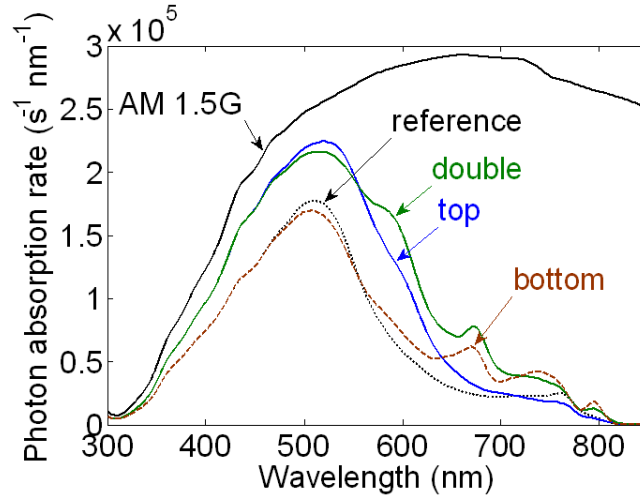


Fig. 11 Photon absorption rates as functions of wavelength in the cases of periodical top Al NC distribution (top), bottom Al NC distribution (bottom), and both top and bottom Al NC distributions (double). In the case of double NCs, the top and bottom NCs are vertically aligned. The curves of the reference condition (no NP) and AM 1.5G are also shown for comparison.

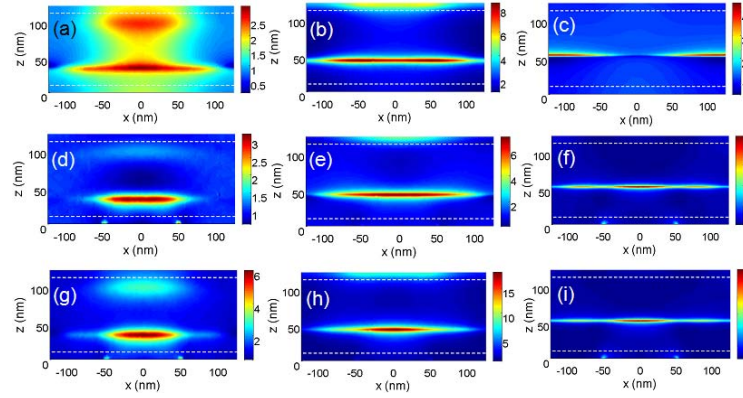


Fig. 12 Distributions of electrical intensity enhancement ratios (over that of the reference case) within the a-Si regions in the x-z plane of the cases in Fig. 11 with (a)-(c) for the cases of top NC, (d)-(f) for the cases of bottom NC, and (g)-(i) for the cases of double NCs. The corresponding wavelengths are 525 nm in (a), (d), and (g), 600 nm in (b), (e), and (h), and 675 nm in (c), (f), and (i). The two horizontal white dashed lines represent the boundaries between the p-type and intrinsic a-Si layers and between the intrinsic and n-type layers.

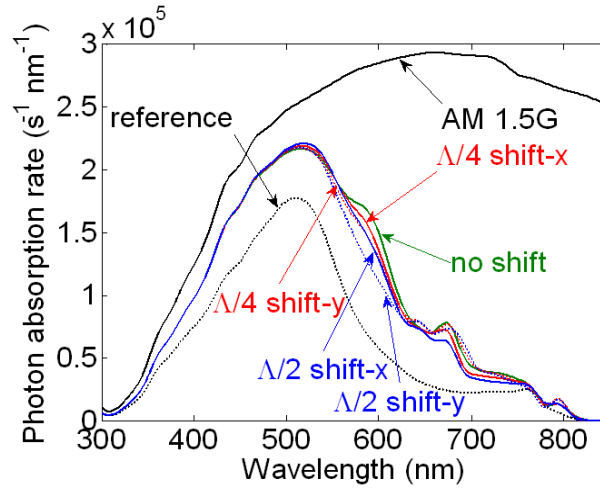


Fig. 13 Photon absorption rates as functions of wavelength in various cases of double Al NCs with the vertical alignment shifted horizontally by one-quarter ($\Lambda/4$ shift) and one-half ($\Lambda/2$ shift) the period (Λ) in the x- and y directions. The incident sunlight is assumed to be x-polarized. The curves of no shift, reference, and AM 1.5G are also shown for comparison.

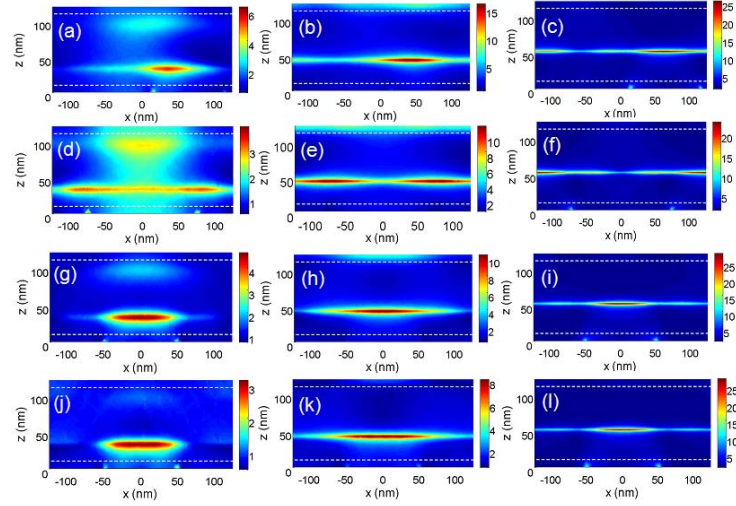


Fig. 14 Distributions of electrical intensity enhancement ratios (over that of the reference case) within the a-Si regions in the x-z plane of the cases in Fig. 13 with (a)-(c) for the case of $\Lambda/4$ shift-x, (d)-(f) for the case of $\Lambda/2$ shift-x, (g)-(i) for the case of $\Lambda/4$ shift-y, and (j)-(l) for the case of $\Lambda/2$ shift-y. The corresponding wavelengths are 525 nm in (a), (d), (g), and (j), 600 nm in (b), (e), (h), and (k), and 675 nm in (c), (f), (i), and (l). The two horizontal white dashed lines represent the boundaries between the p-type and intrinsic a-Si layers and between the intrinsic and n-type layers.

Part III: Surface Plasmon Coupling with a Radiating Dipole

Surface plasmon (SP) coupling with a light emitter for enhancing light emission efficiency is an attractive research topic. It can be used for significantly increasing the emission strength of an originally weakly-emitted molecule. It also has the important application to the efficiency improvement of a light-emitting diode (LED). When a light emitter or radiating dipole is placed near a metallic nanostructure, the induced SP resonance can couple with the dipole and enhance its overall emission efficiency. It is supposed that such a coupling process can increase the radiative transition rate of the radiating dipole. Based on the SP coupling with the electron-hole pairs in the quantum wells (QWs) of an InGaN/GaN QW LED, the LED emission efficiency improvement has been demonstrated [1,2]. To interpret the emission efficiency improvement, numerical studies on such an SP-dipole coupling process have also been reported [3,4]. In such studies, various numerical techniques were used for evaluating the enhanced radiated power when a radiating dipole was placed close to a metal surface or nanostructure. However, those numerical studies were based on the assumption of fixed dipole strength. In other words, the efficiency enhancement is simply due to the additional emission of the equivalent image dipole, represented by the induced SP resonance. Such a coupling picture is incomplete because the induced SP resonance can influence the dipole strength or produce a feedback effect on the dipole radiative transition rate. A more complete simulation model is needed for further understanding the SP-dipole coupling scenarios. In this letter, we numerically study such a feedback effect by assuming a two-level system for the dipole oscillation to achieve a more complete picture of SP-dipole coupling. It is found that the dipole emission power can be further enhanced by including the feedback effect.

In this study, we consider a system consisting of a metal nanosphere (NS) and a nearby radiating dipole, as shown in Fig. 1. The metal NS of R in radius and ϵ_{metal} in dielectric constant is centered at the coordinate origin, i.e., $(0,0,0)$. The dielectric constant of the background medium is ϵ_{out} . The radiating dipole, represented by $\vec{p}_0(\vec{r}, t) = p_0(\bar{p}_{0x}\hat{x} + \bar{p}_{0y}\hat{y} + \bar{p}_{0z}\hat{z})e^{-i\omega t}$, is located at $(0,0,a)$. The electric field of the radiating dipole induces localized surface plasmon resonance (LSPR) on the metallic NS, resulting in a strong near field distribution in its vicinity. It is supposed that such a strong field of LSPR can affect the dipole strength. In other words, the LSPR causes a feedback effect.

A classical dipole corresponds to the electron transition between two energy levels. Here, we use the semi-classical theory for solving the problem of electromagnetic field interaction with a two-level system. Since the size of the NS is much smaller than the radiating wavelength and the interaction occurs essentially in the near field range, the quasistatic approximation is used and the induced electric field can be solved analytically. After certain derivations, the induced electric field at $(0,0,a)$ can be written as

$$\vec{E}(0,0,a) = \bar{p}_{0x}E_0f_x\hat{x} + \bar{p}_{0y}E_0f_y\hat{y} + \bar{p}_{0z}E_0f_z\hat{z} \quad (1)$$

With

$$E_0 = \frac{P_0}{4\epsilon_{\text{out}}\epsilon_0\pi a^3}, \quad (2)$$

$$f_x = f_y = \frac{(\bar{\epsilon} - 1)}{2} \left(\frac{R}{a}\right)^3 \sum_{n=0}^{\infty} \frac{(n+1)(n+2)}{\left(\bar{\epsilon} + 1 + \frac{1}{n+1}\right)} \left(\frac{R}{a}\right)^{2n}, \quad (3)$$

$$f_z = (\bar{\epsilon} - 1) \left(\frac{R}{a}\right)^3 \sum_{n=0}^{\infty} \frac{(n+2)^2}{\left(\bar{\epsilon} + 1 + \frac{1}{n+1}\right)} \left(\frac{R}{a}\right)^{2n}, \quad (4)$$

and

$$\bar{\epsilon} = \frac{\epsilon_{\text{metal}}(\omega)}{\epsilon_{\text{out}}}. \quad (5)$$

To investigate the feedback effect of the LSPR on the two-level system, we solve the optical Bloch equations with the rotating wave approximation and the dipole approximation [5]. For mathematical simplicity, we define $\bar{p}_x = \frac{p_x}{p_0}$, $\bar{p}_y = \frac{p_y}{p_0}$, $\bar{p}_z = \frac{p_z}{p_0}$, and $\xi = |\bar{p}_x|^2|f_x|^2 + |\bar{p}_y|^2|f_y|^2 + |\bar{p}_z|^2|f_z|^2$. Then, we

can derive the governing equations from the steady state solutions of the optical Bloch equations to

give

$$\xi = \frac{|\bar{p}_{0x}f_x|^2}{\left(1 + \frac{Af_x}{1+B\xi}\right)^2} + \frac{|\bar{p}_{0y}f_y|^2}{\left(1 + \frac{Af_y}{1+B\xi}\right)} + \frac{|\bar{p}_{0z}f_z|^2}{\left(1 + \frac{Af_z}{1+B\xi}\right)} \quad (6)$$

and

$$\bar{p}_i = \frac{\bar{p}_{0i}}{\left(1 + \frac{Af_i}{1+B(|\bar{p}_xf_x|^2 + |\bar{p}_yf_y|^2 + |\bar{p}_zf_z|^2)}\right)} \quad (i = x, y, z) \quad (7)$$

where $A = -iT_2 \frac{\mu^2 E_0}{\hbar p_0} e^{2i\left(\frac{na\omega}{c}\right)a}$, $B = \frac{T_1 T_2}{\hbar^2} \mu^2 E_0^2$, T_1 is the spontaneous decay time, T_2 is the dephasing

time, and μ is the dipole matrix element. Once Eq. (6) can be solved, by substituting the solution into Eq. (7), one can obtain the resultant dipole components. The parameters used for numerical calculations include $T_1 = 10^{-9}$ s, $T_2 = 2T_1$, $\mu = 5 \times 10^{-29}$ C·m, $p_0 = 2\mu$, and $\epsilon_{\text{out}} = 6.25$. The Drude model as

$\epsilon_{\text{metal}}(\omega) = 1 - \frac{\omega_p^2}{\omega(\omega + i\gamma)}$ is used for the calculation of frequency-dependent dielectric constant of

the metallic NS. In the following calculations, the metal is assumed to be silver with $\omega_p = 1.19 \times 10^{16}$ rad/s and $\gamma = 1.32 \times 10^{14}$ rad/s and the radius of the NS is set at 10 nm.

Two orientations of the dipole are considered, including one along the z-axis (the z-dipole) and the other along the x-axis (the x-dipole). In both orientations, four locations of the dipole, i.e., $a = 45, 50, 60$, and 70 nm, are considered for simulation. The dipole strength enhancement ratios as functions of wavelength are shown in Figs. 2 and 3 for z- and x-dipole, respectively. Comparing Figs. 2 and 3, one can see that the enhancement ratio, enhanced from the condition of no metal NS, of the z-dipole is larger than that of the x-dipole. The enhancement of dipole strength is about 35% at $a = 50$ nm for the z-dipole and 25% at $a = 45$ nm for the x-dipole. Both Figs. 2 and 3 clearly show two peaks. The peak on the long wavelength side is caused by the induced dipole resonance on the metal NS. The other peak on the short wavelength side corresponds to the induced quadrupole resonance. As the ratio a/R becomes larger, the shorter-wavelength peak diminishes and the longer-wavelength peak asymptotically approaches the resonance condition of a metal NS excited by a uniform plane wave [6].

The total radiated power of the dipole-NS system is also calculated for comparing to the case without the feedback effect. Here, the total radiated power is normalized by the corresponding value of an isolated dipole, $\bar{P}_0 = \frac{p_0^2}{4\pi\epsilon_{\text{out}}\epsilon_0} \cdot \left(\frac{n^3\omega_{\text{LSP}}^4}{3c^3}\right)$, where n is the refractive index of the background

medium, which is set at 2.5 by assuming that the dipole and NS are embedded in GaN, and $\omega_{\text{LSP}} = 3.24 \times 10^{15}$ rad/s is the LSPR frequency of a metal NS excited by a uniform plane wave. The numerical results are shown in Figs. 4 and 5 for the z- and x-dipole, respectively. Here, one can first see that with the feedback effect, the total radiated power at either dipole or quadrupole resonance is significantly more enhanced, when compared with the case of no feedback. Also, at either resonance, the total radiated power is generally more enhanced in the case of the z-dipole, when compared with the case of the x-dipole. When $a = 45$ nm, the inclusion of the feedback effect results in more resonant enhancement of the total radiated power by ~80 and ~72 % for the z- and x-dipole, respectively. The total radiated power enhancement ratios of the feedback case over the non-feedback case as functions of wavelength with the z- and x-dipole are shown in Figs. 6 and 7, respectively. One can see that by including the feedback effect, the enhancement is significantly increased.

In summary, we have demonstrated the simulation results of the enhanced radiated power of a radiating dipole when it was coupled with the LSPR of a nearby metal NS by including the influence of the LSPR on the strength of the dipole, which was represented by a two-level system in our semi-classical model. It was shown that with this feedback influence, the total radiated power could be further enhanced by more than 70 %, when compared with the condition of ignoring the feedback effect. In comparing the results of two different dipole orientations, it was discovered that at a fixed distance from the metal NS, the radial dipole orientation led to more significant enhancement of total

radiated power, when compared to the orbital dipole orientation.

References:

1. D. M. Yeh, C. F. Huang, C. Y. Chen, Y. C. Lu, and C. C. Yang, *Nanotechnology* **19**, 345201 (2008).
2. C. F. Lu, C. H. Liao, C. Y. Chen, C. Hsieh, Y. W. Kiang, and C. C. Yang, *Appl. Phys. Lett.* **96**, 261104 (2010).
3. J. Y. Wang, Y. W. Kiang, and C. C. Yang, *Appl. Phys. Lett.* **91**, 233104 (2007).
4. W. H. Chuang, J. Y. Wang, C. C. Yang, and Y. W. Kiang, *IEEE Photon. Technol. Lett.* **20**, 1339 (2008).
5. L. Allen and J. H. Eberly, *Optical resonance and two-level atoms*, Dover, New York (1987).
6. S. A. Maier, *Plasmonics*, Springer, Berlin (2007).

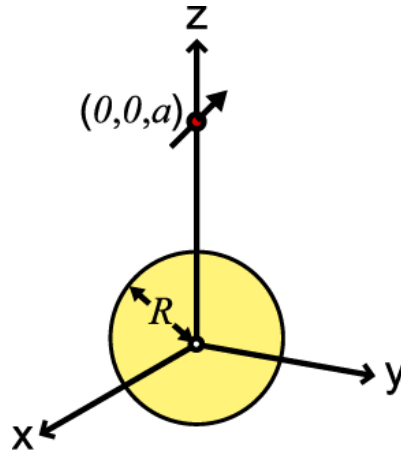


Fig. 1 configuration of the simulation system, consisting of a metal NS with radius R , centered at $(0,0,0)$, and a radiating dipole located at $(0,0,a)$.

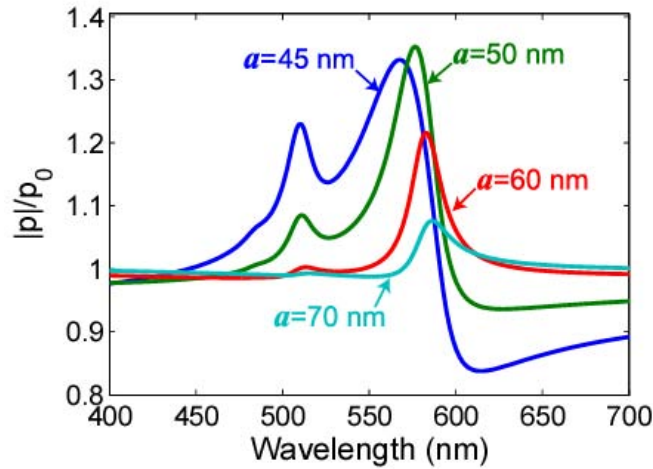


Fig. 2 Wavelength dependencies of the strength of the z-dipole at various dipole-NS distances.

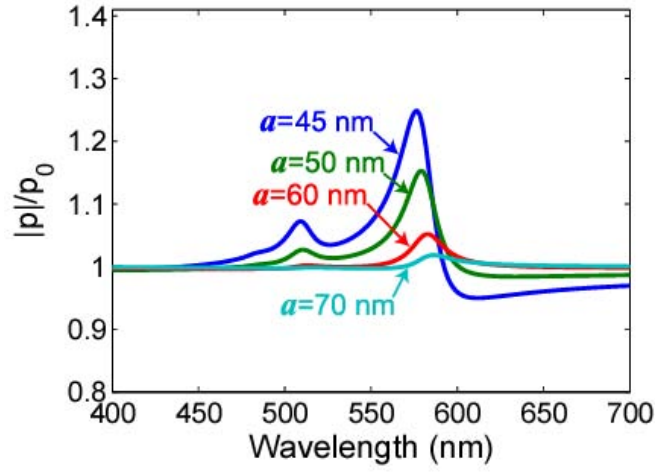


Fig. 3 Wavelength dependencies of the strength of the x-dipole at various dipole-NS distances.

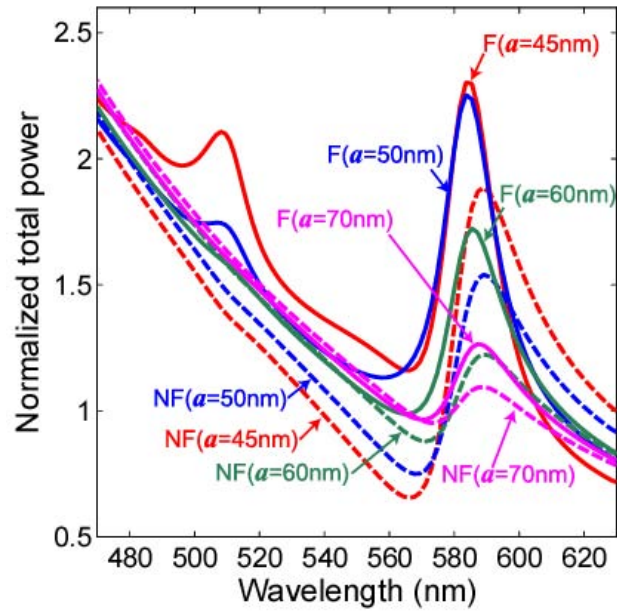


Fig. 4 Wavelength dependencies of the normalized total radiated power of the z-dipole at various dipole-NS distances, including the conditions with (F) and without (NF) the feedback effect.

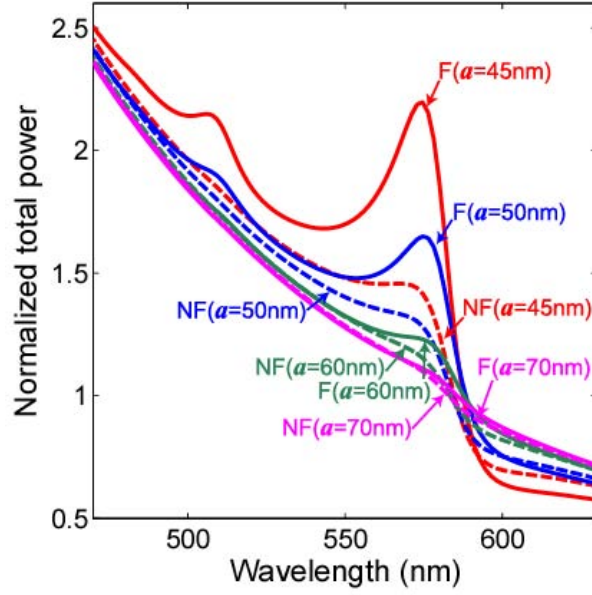


Fig. 5 Wavelength dependencies of the normalized total radiated power of the x-dipole at various dipole-NS distances, including the conditions with (F) and without (NF) the feedback effect.

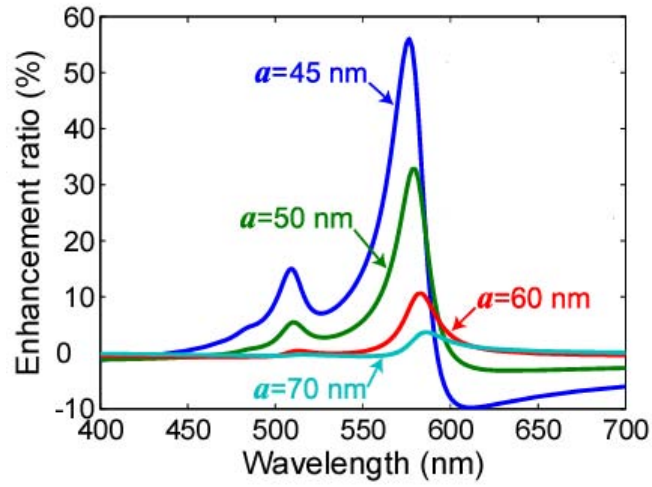


Fig. 6 Total radiated power enhancement ratios of the feedback case over the non-feedback case as functions of wavelength with the z-dipole.

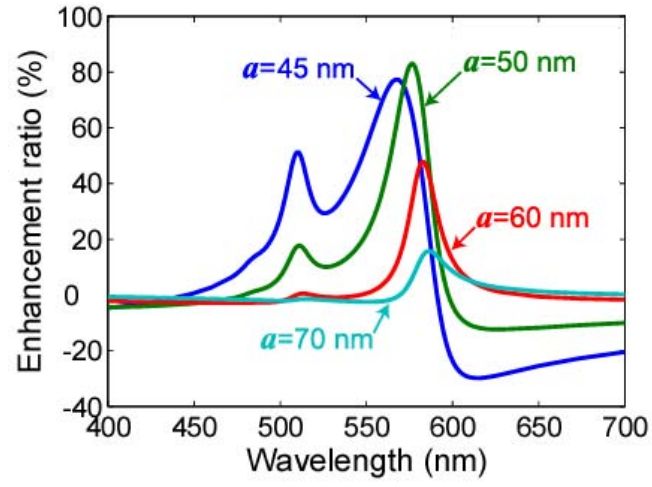


Fig. 7 Total radiated power enhancement ratios of the feedback case over the non-feedback case as functions of wavelength with the x-dipole.

List of Journal Publications Directly Related to the Proposal Contents:

1. Jyh-Yang Wang, Fu-Ji Tsai, Yean-Woei Kiang, and C. C. Yang, “Enhancing InGa_N-based Solar Cell Efficiency through Localized Surface Plasmon Interaction by Embedding Ag Nanoparticles,” *Opt. Express*, Vol. 18, No. 3, p. 2682~2694, 1 February 2010.
2. Fu-Ji Tsai, Jyh-Yang Wang, Yean-Woei Kiang, and C. C. Yang, “Absorption enhancement of an a-Si solar cell through metal nanoparticle scattering,” *Optics Express* Vol. 18, Iss. S2, pp. A207–A220, 2010.
3. Hung-Yu Tseng, Cheng-Kuang Lee, Shou-Yen Wu, Ting-Ta Chi, Kai-Min Yang, Jyh-Yang Wang, Yean-Woei Kiang, C. C. Yang, Meng-Tsan Tsai, Yang-Che Wu, Han-Yi E. Chou, and Chun-Pin Chiang, “Au Nanorings for Enhancing Absorption and Backscattering Monitored with Optical Coherence Tomography,” *Nanotechnology*, Vol 21, p. 295102, 2010.
4. Kun-Ching Shen, Che-Hao Liao, Zan-Yao Yu, Jyh-Yang Wang, Cheng-Hung Lin, Yean-Woei Kiang, and C. C. Yang, “Effects of the intermediate SiO₂ layer on polarized output of a light-emitting diode with surface plasmon coupling,” *Journal of Applied Physics*, Vol. 108, Issue 11, p. 113101-1~8, 1 Dec. 2010.

List of Other Journal Publications Acknowledging the Supports of This Contract:

1. Cheng-Hung Lin, Chih-Yen Chen, Che-Hao Liao, Chieh Hsieh, Yean-Woei Kiang, and C. C. Yang, “Fabrication of Vertical Light-emitting Diode Based on Sapphire Substrate Liftoff with Photoelectrochemical Etching,” accepted for publication in *IEEE Photonics Technology Letters*.
2. Cheng-Hung Lin, Jyh-Yang Wang, Cheng-Yen Chen, Kun-Ching Shen, Dong-Ming Yeh, Yean-Woei Kiang, and C. C. Yang, “Ga_N Photonic Crystal Membrane Laser,” *Nanotechnology*, Vol. 22, p. 025201, 2011.
3. Cheng-Kuang Lee, Hung-Yu Tseng, Chia-Yun Lee, Shou-Yen Wu, Ting-Ta Chi, Kai-Min Yang, Han-Yi Elizabeth Chou, Meng-Tsan Tsai, Jyh-Yang Wang, Yean-Woei Kiang, Chun-Pin Chiang, and C. C. Yang, “Characterizing the localized surface plasmon resonance behaviors of Au nanorings and tracking their diffusion in bio-tissue with optical coherence tomography,” *Biomedical Optics Express*, Vol. 1, No. 4, pp.1059-1073, Nov. 1, 2010. Also selected to publish in *Spotlight on Optics*, an OSA feature that highlights select articles each month from the OSA flagship journals.
4. Chih-Feng Lu, Che-Hao Liao, Chih-Yen Chen, Chieh Hsieh, Yean-Woei Kiang, and C. C. Yang, “Reduction of the efficiency droop effect of a light-emitting diode through surface plasmon coupling,” *Applied Physics Letters*, Vol. 96, 261104 June 30, 2010.
5. Cheng-Hung Lin, Cheng-Yen Chen, Dong-Ming Yeh, and C. C. Yang, “Light extraction enhancement of a Ga_N-based light-emitting diode through grating-patterned photoelectrochemical surface etching with phase mask interferometry,” *IEEE Photonics Technology Letter*, Vol. 22, Issue 9, pp. 640-642, May, 2010.
6. Tsung-Yi Tang, Wen-Yu Shiao, Yung-Sheng Chen, Cheng-Hung Lin, Wen-Ming Chang, Che-Hao Liao, Kun-Ching Shen, C. C. Yang, Ming-Chi Hsu, Jui-Hung Yeh, and Ta-Cheng Hsu, “Nitride Nanocolumns for the Development of Light-emitting Diode,” *IEEE Transactions on Electron Devices*, vol. 57, no. 1, pp. 71-78, January 2010. (invited)

Future Work:

1. Fabrication of metal nanorings of various geometries and understanding their localized surface plasmon behaviors

We will continue the use of nanosphere lithography and metal secondary sputtering methods for fabricating Au nanorings of various ring diameters and heights. The goal is to control the localized surface plasmon resonance wavelength and strength for covering a spectral range from visible through near-infrared. Various measurement methods will be used for understanding their resonance behaviors.

2. Comparison of localized surface plasmon behaviors between Au nanoring, nanoshell, and nanorod

We will continue the cooperation with Professor Randall Lee of Houston University and Professor C. Y. Mou of National Taiwan University for comparing the localized surface plasmon behaviors of our Au nanorings with their nanoshells and nanorods. The effects of coated porous SiO₂ layer on localized surface plasmon resonance behaviors will also be studied.

3. Experimental study of surface plasmon coupling with a dipole through cathodoluminescence measurement

For either emission or absorption (detection or imaging) application, the fundamental behavior of surface plasmon coupling with an emitting or absorber needs to be understood. The simplest method for this study is photoluminescence. However, in such a study, the excitation strength depends on the sample structure and the result becomes unreliable. In a cathodoluminescence measurement, luminescence is excited by incident electron. Such electron excitation is weakly related to sample structure for more accurately understanding the coupling behavior.

4. Further numerical study of surface plasmon coupling with a dipole

We will study the coupling behaviors of one surface plasmon mode with more than one dipole to see the effects of coherent coupling and emission. If such a multiple-dipole coherent coupling can be implemented, even stronger enhancements of emission and absorption through surface plasmon coupling can be implemented.

5. Further numerical study of surface plasmon enhanced solar cell

We will further numerically study the absorption enhancement effect of a silicon solar cell with metal nanostructures to optimize the design of such a solar cell. Hopefully, we can receive equipment for implementing such a silicon solar cell in the near future.